

**EFFECT OF PARTICLE ANISOTROPY ON SUSPENSION RHEOLOGY AND
PHASE BEHAVIOR WITH TUNABLE ATTRACTIVE STRENGTH**

by

Yun Soo Kim

A thesis submitted to the Faculty of the University of Delaware
in partial fulfillment of the requirements for the degree of
Master of Chemical Engineering

Winter 2015

© 2015 Yun Soo Kim
All Rights Reserved

UMI Number: 1585157

All rights reserved

INFORMATION TO ALL USERS

The quality of this reproduction is dependent upon the quality of the copy submitted.

In the unlikely event that the author did not send a complete manuscript and there are missing pages, these will be noted. Also, if material had to be removed, a note will indicate the deletion.



UMI 1585157

Published by ProQuest LLC (2015). Copyright in the Dissertation held by the Author.

Microform Edition © ProQuest LLC.

All rights reserved. This work is protected against unauthorized copying under Title 17, United States Code



ProQuest LLC.
789 East Eisenhower Parkway
P.O. Box 1346
Ann Arbor, MI 48106 - 1346

**EFFECT OF PARTICLE ANISOTROPY ON SUSPENSION RHEOLOGY AND
PHASE BEHAVIOR WITH TUNABLE ATTRACTIVE STRENGTH**

by

Yun Soo Kim

Approved: _____
Norman J. Wagner, Ph.D.
Professor in charge of thesis on behalf of the Advisory Committee

Approved: _____
Abraham M. Lenhoff, Ph.D.
Chair of the Department of Chemical and Biological Engineering

Approved: _____
Babatunde A. Ogunnaike, Ph.D.
Dean of the College of Engineering

Approved: _____
James G. Richards, Ph.D.
Vice Provost for Graduate and Professional Education

ACKNOWLEDGMENTS

This work would not have been possible without the advice and support of many people.

First and foremost, I would like to thank my advisor, Dr. Norm Wagner for providing me with the opportunity and guidance throughout this project. I truly appreciate his tireless effort and devotion throughout my graduate research experience.

I also received much help from former and current Wagner group members in one way or another and would like to thank them by taking advantage of this opportunity. Especially, Rose Ndong helped me very much when I joined the group and taught me particle synthesis technique that is being used in this dissertation. Jung Min Kim is another person that I truly appreciate for the valuable discussion with him. Thanks to Jingsi for her kind help with various experiment techniques. I would like to thank Rich and Colin for helping me with the rheometer and valuable discussions. I also want to thank Dan Greene as he always gave me valuable suggestions on anisotropic particle behavior. Thanks to Simon for insightful and delightful discussions on my project. Thanks to Doug Godfrin, Stephen Ma, Paul Mwasame, Michelle Calabrese, Matt Amstrong, Melissa Gordon, Ru Chen for being helpful labmates in Colburn Lab. I also thank to Paul Butler, Yun Liu and Matt Wasbrough, at NCNR and Lilin He at Oak Ridge for their help with neutron scattering measurement setup and data analysis. I also express my thanks to Frank Kriss and Jan sloppy for training with TEM. Finally, I would like to thank my parents and sister who's love and encouragement gave me the strength during master years.

TABLE OF CONTENTS

| | |
|----------------------|-----|
| LIST OF TABLES..... | vi |
| LIST OF FIGURES..... | vii |
| ABSTRACT..... | x |

Chapter

1 INTRODUCTION

| | |
|---|----|
| 1.1 Motivation..... | 1 |
| 1.2 Background..... | 2 |
| 1.2.1 Adhesive hard particles: colloidal dispersions with attractive interactions..... | 2 |
| 1.2.2 Phase behavior of Adhesive Hard Spheres (AHS)..... | 3 |
| 1.2.3 Flow behavior of Adhesive Hard Sphere (AHS)..... | 6 |
| 1.3 Phase Behavior of Dispersions of Anisotropic Particles..... | 7 |
| 1.3.1 Rod-like particles..... | 7 |
| 1.3.2 Pair potential driven self-assembly..... | 8 |
| 1.3.3. Anisotropic particles flow behavior..... | 10 |
| 1.4 Objectives and Overview..... | 11 |

2 EXPERIMENTAL METHODS..... 13

| | |
|---|----|
| 2.1 Dynamic Light Scattering (DLS)..... | 13 |
| 2.2 Transmission Electron Microscopy (TEM)..... | 13 |
| 2.3 Rheometry..... | 14 |
| 2.4 Small-angle Neutron Scattering (SANS)..... | 15 |
| 2.4.1 Static-SANS..... | 17 |
| 2.4.2 Rheo-SANS..... | 17 |

3 THEORETICAL CALCULATION OF VAN DER WAALS FORCES FOR CORE-SHELL ELLIPSOIDAL PARTICLES..... 19

| | |
|---|----|
| 3.1 Orientation Dependent van der Waals Force..... | 19 |
| 3.2 Calculation of van der Waals Force of Core-shell Ellipsoid..... | 22 |

| | | |
|-------|---|----|
| 4 | PARTICLE SYNTHESIS AND CHARACTERIZATION..... | 28 |
| 4.1 | Particle Synthesis..... | 28 |
| 4.1.1 | Synthesis of ellipsoidal TiO ₂ particles..... | 28 |
| 4.1.2 | Silica coating..... | 31 |
| 4.1.3 | Effect of PVP molecular mass..... | 32 |
| 4.1.4 | Octadecyl polymer brush grafting onto SiO ₂ -TiO ₂ surface..... | 35 |
| 4.2 | Particle Characterization..... | 36 |
| 4.2.1 | Particle geometry (TEM)..... | 36 |
| 4.2.2 | Characterization by SANS..... | 37 |
| 5 | RHEOLOGICAL RESULTS AND DISCUSSION..... | 40 |
| 5.1 | Preshear..... | 41 |
| 5.2 | Temperature Sweep..... | 42 |
| 5.3 | Frequency Sweep..... | 43 |
| 5.4 | Comparison Of The Gel Temperature With Spherical System..... | 45 |
| 6 | SMALL-ANGLE NEUTRON SCATTERING RESULTS AND DISCUSSION..... | 49 |
| 7 | CONCLUSIONS AND FUTURE DIRECTION..... | 52 |
| 7.1 | Conclusion..... | 52 |
| 7.2 | Future Direction..... | 54 |
| | REFERENCES..... | 56 |
| | Appendix | |
| | NOMENCLATURE AND ACRONYMS..... | 63 |

LIST OF TABLES

| | | |
|------------------|--|----|
| Table 3.1 | Equations of van der Waals energy between two rod-like particles in different geometries and corresponding spheres in terms of their Hamaker constant, A and surface to surface separation distance D..... | 20 |
| Table 3.2 | Parameters used for the calculations of van der Waals energy..... | 21 |
| Table 4.1 | Properties of ellipsoidal TiO ₂ core particle..... | 31 |
| Table 4.2 | Properties of Adhesive hard ellipsoid particles..... | 37 |
| Table 4.3 | SANS modeling for bare TiO ₂ in D ₂ O..... | 38 |

LIST OF FIGURES

| | | |
|-------------------|---|----|
| Figure 1.1 | Change in the conformation of the solvent molecules (blue line) and the grafted chain (black line) at (a) 40°C and (b) 25°C on the silica surface. The figure is reprinted with permission from [22]. Copyright 2010 American Chemical Society..... | 3 |
| Figure 1.2 | State diagram for the model adhesive hard sphere systems showing the gel line transition. The green points the experimentally determined dynamical arrest transition. The broken line is the analytical solution to the percolation line using the Percus–Yevick approximation. Reprinted figure with permission from [1]. Copyright 2011 by the American Physical Society..... | 4 |
| Figure 1.3 | Map of the volume fraction and aspect ratio r dependences of rod gels and glasses. The figure is adapted from [5] with permission of The Royal Society of Chemistry (RSC)..... | 9 |
| Figure 1.4 | Comparison of the q -dependent scattering intensity, $I(q)$, for the limiting cases of rod suspension structure: homogeneous rigid rod networks and heterogeneous rod fractal clusters. The figure is adapted from [5] with permission of The Royal Society of Chemistry (RSC)..... | 10 |
| Figure 2.1 | Rheo SANS shear cell configuration..... | 18 |
| Figure 3.1 | Orientation-dependent van der Waals interactions of two rod-like particles of aspect ratio 4.78 as a function of surface to surface separation distance (nm). The values are also given for corresponding spheres ($r=32\text{nm}$) of equivalent volume..... | 22 |
| Figure 3.2 | Individual components of the van der Waals interactions of a core-shell ellipsoids in parallel orientation. Image courtesy of Jung Min Kim..... | 23 |
| Figure 3.3 | Geometry of ellipsoids with different radius in prolate spheroidal Coordinates..... | 24 |
| Figure 3.4 | van der Waals interactions of core-shell spherical silica-coated TiO_2 with different silica shell thickness. Solid and dotted lines correspond to surface-surface distance taking into account octadecyl brush height at low temperature and high temperature, | |

| | | |
|-------------------|--|----|
| | respectively..... | 26 |
| Figure 4.1 | A schematic of the model anisotropic particle consisted of ellipsoidal TiO ₂ particle as the core coated with a silica shell with octadecyl chain grafting on the surface (not to scale). The particle geometry is idealized as a sphereocylinder for purposes of showing the particle's layered structure..... | 28 |
| Figure 4.2 | Transmission electron micrograph of ellipsoidal TiO ₂ particles synthesized through gel-sol synthesis..... | 30 |
| Figure 4.3 | Effect of TEOS addition for the silica-coating process on mean particle diameter, as measured from TEM images and calculated theoretically..... | 33 |
| Figure 4.4 | TEM micrographs of TiO ₂ coated with silica after coated with PVP-54k (a) and PVP-10k (b)..... | 34 |
| Figure 4.5 | Transmission electron microscope images of SiO ₂ -TiO ₂ particles..... | 37 |
| Figure 4.6 | Intensity vs. scattering vector for bare TiO ₂ in D ₂ O..... | 38 |
| Figure 5.1 | Suspension viscosity during preshearing at 500s ⁻¹ for 60 seconds at the beginning and between measurements. All measurements performed at 20 °C..... | 41 |
| Figure 5.2 | Temperature ramp measurement of 6 vol% AHE suspension at an oscillatory frequency of 1 rad/s and temperature ramp rate of 0.2°C/min..... | 42 |
| Figure 5.3 | Temperature dependence of tetradecane | 43 |
| Figure 5.4 | Frequency sweep measurements of 6 vol% AHE dispersion from 13°C to 15°C..... | 44 |
| Figure 5.5 | (a) Gel temperature comparison of three different particle sizes as a function of volume fraction. The data for spheres are adapted from [64]. (b) Crystallization temperature of a mixture of 1-octadecanol and n-tetradecane as a function of mole fraction of 1-octadecanol. The figure is reprinted from [64]..... | 46 |
| Figure 5.6 | Ascending and descending shear stress sweeps performed for 6vol% AHE suspension..... | 48 |

| | | |
|-------------------|--|----|
| Figure 6.1 | (a) 1-D SANS intensity curves of a dispersion of 6 vol% AHE particles in <i>n</i> -tetradecane from 10°C to 30°C. (b) Zoom-in of the low <i>q</i> region. Note: The data at 20°C (purple points) are almost exactly overlapped on the data at 14°C (Red points). Hence the data at 14°C are not visible..... | 50 |
| Figure 7.1 | 3D Proposed 3D state diagram for the adhesive hard ellipsoid model system (right) similar to that of isotropic system [6] (left) τ , ϕ , and α indicate Baxter parameter, volume fraction, and particle anisotropy, respectively..... | 55 |

ABSTRACT

Particle shape plays a very important role in the thermodynamic and rheological properties of colloidal and nanoparticle suspensions and new phenomena arise as compared to dispersions of isotropic particles. Previously, a state diagram has been constructed for the simplest, fundamental system that includes both excluded volume and attractive interparticle interactions, *i.e.*, adhesive hard spheres. This was performed by combining state-of-the-art simulations, rheology and small angle neutron scattering (SANS) experiments on a model dispersion [1]. In this study, we extend the state diagram to include shape effects by characterizing the dynamical arrest and strength of attraction of model adhesive hard spheres (AHS) comprised of octadecyl-grafted silica nanoparticles in n-tetradecane. We synthesize model, anisotropic colloidal particles of aspect ratio 2.5 ± 0.4 by first by growing ellipsoidal titanium dioxide particles as the core and then coating these templates with a silica shell. The silica coating layer was added to achieve the same surface chemistry as the previous isotropic systems and to reduce the strong van der Waals attractions induced by the titanium cores. Octadecyl chains are grafted onto the silica coating as done previously for the spherical analogs to develop a system exhibiting thermoreversible gelation. Gel temperatures were determined by dynamic oscillatory rheological measurements whereas SANS experiments performed in the vicinity of the rheological gel temperature provided microstructural information. The rheological results shows the adhesive hard ellipsoids suspension formed a gel-like structure as determined by

applying the Winter and Chambon criterion [2] SANS results show a more compact structure is formed in comparison with the structure of the aggregates formed by spherical particles of comparable size. The results show that the phase behavior strongly depends on particle shape at a given particle volume fraction and provide guidance for the formulation of gels of anisotropic colloidal particles.

Chapter 1

INTRODUCTION

1.1 Motivation

Suspensions of anisotropic particles, such as clays, pigments, and inorganic mineral crystals are important in the formulation of chemicals, pharmaceuticals, paints, and coatings. They exhibit different and intriguing phenomena in suspension rheology as compared with dispersions of isotropic particles [3] because, among other reasons, anisotropic particles can be rotated and oriented by flow fields. In general, suspensions of anisotropic particles show much stronger elasticity and solid-like rheological properties at lower volume fractions than their isotropic counterparts [4, 5]. This can be understood because anisotropic particles have a larger surface to volume ratio and therefore, can form more contacts with neighboring particles than for spherical particles at comparable volume fractions. Particle anisotropy dramatically affects the equilibrium microstructure and phase behavior as well. For instance, it can shift the glass and gel transition lines in the state diagram to much lower volume fractions [5]. Furthermore, deviations from a spherical shape introduce distinguishing phase behaviors not observed for spherical particle suspensions such as liquid crystalline phases.

Although many distinguishing characteristics of anisotropic particle suspensions have been reported in literature [3-7], comparatively few studies provide a systematic, quantitative investigation on the influence of particle anisotropy on gelation or gel rheology. Currently, the transition between the gel and glass states and the change in rheological properties of anisotropic particle systems are not fully understood. Specifically, the effect of aspect ratio on the relationship between attraction strength, and particle volume fraction that defines the gel and glass states is still unknown, while isotropic systems have been systematically studied [1, 8]. Eberle et al. [1] constructed the state diagram for a system of adhesive hard spheres (AHS) by

combining Monte Carlo simulations, rheology, and small-angle neutron scattering (SANS) experiments on a model dispersion. In the current project, we aim to extend the previous work to an anisotropic system comprised of particles described as prolate ellipsoids of revolution of moderate aspect ratio¹ and thereby, extend the AHS state diagram to include adhesive hard ellipsoids (AHE).

1.2 Background

1.2.1 Adhesive hard particles: colloidal dispersions with attractive interactions

Colloidal dispersions that interact via short-ranged attractive potential have a rich and complex phase behavior [9-11]. Of specific interest are the states and phase transitions driven by attractions such as gelation and attractive driven glass (ADG). Numerous experimental and theoretical studies have focused on this behavior [11-14]. One of the most frequently studied model system is the octadecyl-coated thermoreversible adhesive hard-sphere particles [1, 8, 15-21].

The system is composed of a spherical silica core with grafted octadecyl chains on the surface [23]. When the particles are dispersed in the medium of linear hydrocarbon chains such as tetradecane, the particles exhibit a temperature dependent interaction that varies from short-range repulsion to short-range attraction such that suspensions of these particles exhibit thermoreversible gelation. The strength of interparticle attraction can be controlled by temperature and the range of the attraction is set by the thickness of the layer of grafted alkane chains.

¹ In this thesis we will use the conventional scientific usage of "ellipsoid" to mean prolate ellipsoid of revolution.

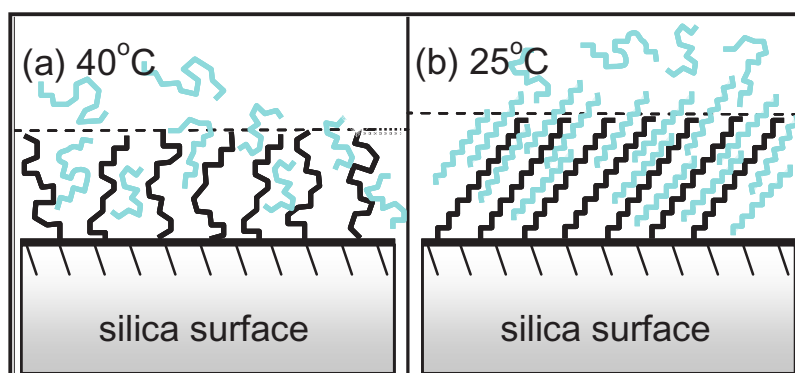


Figure 1.1 Change in the conformation of the solvent molecules (blue line) and the grafted chain (black line) at (a) 40°C and (b) 25°C on the silica surface. The figure is reprinted with permission from [22]. Copyright 2010 American Chemical Society.

Eberle et al. characterized the conformational change of the grafted chains in n-tetradecane as a function of temperature with neutron reflectometry to determine the mechanism for the change from repulsion to attraction [22]. As shown in Figure 1.1, they demonstrated that the chains become linear at low temperatures and promote interdigitated with n-tetradecane molecules, which results in a crystalline phase. At high temperatures, on the other hand, chains fluidize and the crystalline phase disappears. Eberle et al. also prepared a silica substrate coated with the same brush layer material and used neutron reflectivity to see how the scattering length density of the brush layer varies as a function of depth at different temperatures [22]. A similar finding through sum frequency generation spectroscopy was published by Roke et al [24].

1.2.2 Phase behavior of Adhesive Hard Sphere (AHS)

The phase behavior of model AHS particles is reported in Ref. [1] as shown in Figure

1.2. The bold black line corresponds to the binodal transition calculated by using grand canonical Monte Carlo simulations with the critical point denoted by the red star [25]. Gels inside the vapor-liquid binodal boundary are metastable with respect to fluid-solid coexistence [26]. The broken line is an analytical solution of dynamic percolation as determined by the Percus-Yevick approximation [14]. The grey region defines the liquid-crystal transition, which is suppressed as the particles are slightly polydisperse. The repulsion-driven and attraction-driven glass transition lines with the singularity point denoted by A_3 are obtained from the mode-coupling theory [26]. Eberle et al. presented a quantitative, experimental study documenting the gel transition as shown in Figure 1.2 for dispersions of octadecyl grafted silica particles in n-tetradecane, which exhibits a phase transition between liquid and solid as a function of temperature. At high temperatures, the osmotic pressure exerted by the brush layer promotes a steric hindrance and prohibits particle aggregation while the crystallization of the brush layer at low temperatures leads to a contact aggregation between particles.

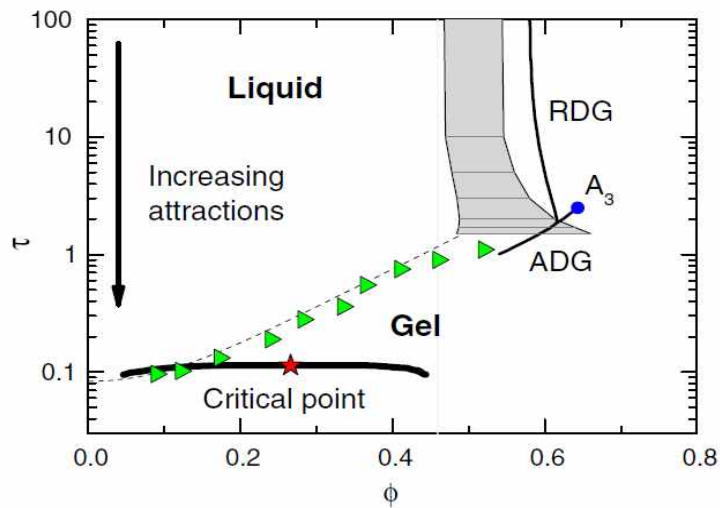


Figure 1.2 State diagram for the model adhesive hard sphere systems showing the gel line transition. The green points the experimentally determined dynamical arrest transition. The broken line is the analytical solution to the percolation line using the Percus–Yevick approximation. Reprinted figure with permission from [1]. Copyright 2011 by the American Physical Society.

The gel temperature is determined by multiple methods, including rheology and dynamic light scattering. Importantly, the gel temperature was determined to within 0.1 °C by identifying a power-law regime over a decade or more of frequency in the dynamic moduli using the so-called Winter- Chambon gel criterion [2]. Then, the gel strength, as represented by the AHS stickiness (or Baxter) parameter, was measured at the rheologically determined gel temperature by fitting the structure factor from static small-angle neutrons scattering measurements with the Ornstein-Zernike equation combined with the Percus-Yevick closure [14]. Figure 1.2 shows the results of this procedure as the green triangles spanning a broad range of volume fractions. As shown, lower attraction strength is necessary to gel the particles at higher particle concentrations. Further, the gel line clearly lies in the one phase region for all but the lowest volume fractions. Close inspection shows the data lies just slightly below the predicted dynamic percolation line, and a more detailed analysis demonstrates that the data follow the predictions of rigidity percolation [27].

Eberle, Fang, Kim and coworkers performed a systematic analysis of the effect of the range of attraction on the phase transition of attractive systems to work towards a common theory for the physical understanding of the adhesive hard sphere [1]. Kim et al. reported the effect of particle size on the dynamic arrest of adhesive hard sphere system with the systematically varying particle size such that the relative range of attraction is reduced for larger particles [16]. Based on Noro and Frenkel's law of corresponding states for systems with short range attractions, Kim et al. expected a universal gel line for systems with relatively narrow ranges of attraction (e.g. $\sim 10\%$ of the particle size). Through the study of a range of particle sizes, they constructed a state diagram showing three distinct regions with different trends concerning the range of attraction. At low volume fractions, the smallest particles can form a stable gel even in the two-phase region without a sign of macroscopically visible phase separation, while the other two systems of larger particles phase separate. Also, at intermediate volume fractions, a systematic shift in the gel line towards a stronger attraction for

larger particles is seen. Finally, the gel line converges to the attractive-driven glass line regardless of the particle size at high concentrations.

The size-dependence of the gel stability can be understood as a consequence of particle aggregation that is in competition with gravitational settling. The threshold of the volume fraction at which particles form a stable homogenous gel appears to be particle size-dependent. The origin of the difference was successfully described within the framework of the gravitational Péclet number Pe_g . By systematically varying the particle size, volume fraction, and the gravitational acceleration via centrifugation, a critical Pe_g was determined that separated stable, homogenous gels from gravitationally induced phase separation. This work elucidated the important role of gravity in the competition between phase separation and gelation in colloidal dispersions at low volume fractions (e.g., below the critical concentration).

1.2.3 Flow behavior of Adhesive Hard Sphere (AHS)

The flow behavior of Adhesive Hard Sphere (AHS) have been recently explored and reviewed in the literature [28]. Eberle et al. reported the microstructure of AHS gels under steady shear at different temperatures and concentrations. They argued that the flow behavior in the fluid and gel states can be characterized by a universal behavior. The concept is based on the competition between the forces driving particle attraction and the force of the shear flow exerted on particles. Thus, rescaling the shear rate with the maximum attractive force acting between particles that accounts for the dependence of temperature, particle concentration, and particle size, Eberle et al. scaled shear rates by introducing M' , which balances the breakdown force of flow with the maximum attractive interparticle force.

$$M' = \frac{6\pi\mu a^2 \dot{\gamma}}{F_{\max}} \quad (1.1)$$

Due to the difficulty in determining the maximum attractive interparticle force, a surrogate, measurable property was substituted. The maximum attractive interparticle force can be expressed in terms of the measurable yield stress as:

$$\tau_y \sim \frac{\phi^2}{a^2} \left(\frac{d\Phi}{dr} \right)_{\max} \quad (1.2)$$

Thus M' can be expressed as

$$M' \sim c \frac{\mu_s \gamma \phi^2}{\tau_y} \quad (1.3)$$

where c is an empirical constant. A limiting behavior of $M' \sim 1$ corresponds to a fluidized suspension where the shear flow is sufficient to pull particle pairs apart. This is taken to be a shear rate of 1000s^{-1} whereupon structure measurements show the particle arrangement is dominated by the shear flow [26].

1.3 Phase Behavior of Dispersions of Anisotropic Particles:

1.3.1 Rod-like particles

Many industrially significant suspensions contain anisotropic particles with simple axisymmetric geometries including rod-like or prolate particles. Colloidal rod suspensions are ubiquitous from inorganic materials (e.g. boehmite and hematite) to fibers such as cellulose. For industrial application, such as photonic materials, the crystalline phases of rod-like particles are interesting targets for self-assembly. Studies of the phase behavior or self-assembly of rod-like particles have a long history since the experiments of Langmuir [9] and the theory of Onsager [29]. The nematic phase is generated due to competition between translational and orientational contributions to the free energy in rod-like particle system [30]. For hard spherocylinders, initial simulations showed that higher particle concentrations lead to a phase transition to the smectic phase, followed at higher concentrations by an oriented crystal [31]. As

concentration is increased, prolate spheroids exhibit only the isotropic–nematic transition [32].

The ordered phases of rods are of interest because their maximum density is higher than that of spheres. For example, the maximum volume fraction of a close-packed ellipsoids with a unit cell of two particles is $\phi_{\max}=0.771$, a value greater than the FCC packing fraction of spheres ($\phi_{\max}=0.7405$) [33]. It is shown that a simple monoclinic phase with a unit cell of two hard prolate spheroids with unequal orientation is more stable than a stretched FCC crystal by using Monte Carlo simulation [34, 35]. Experimental reports of orientationally ordered packings of prolate spheroid at $\phi=0.55$ are quantified as nematic order [36].

1.3.2 Pair potential driven self-assembly

Anisotropic particles can be self-assembled into bulk colloidal phase as a function of colloid volume fraction, pair potential strength, as well as potential range. Systematic experimental exploration of phase behavior of suspensions of anisotropic particles is possible and the anisotropic pair potentials can be parameterized. Such a study of self-assembly under carefully controlled conditions of specified thermodynamic parameters has been reported in the area of colloidal rod and disk assembly [37]. These systems have demonstrated the existence of columnar phases in disk suspensions and a rich sequence of liquid crystal phases in fd-virus. Dogic et al. explored the phase boundaries of colloidal rods that occur as attractions between the rods [38].

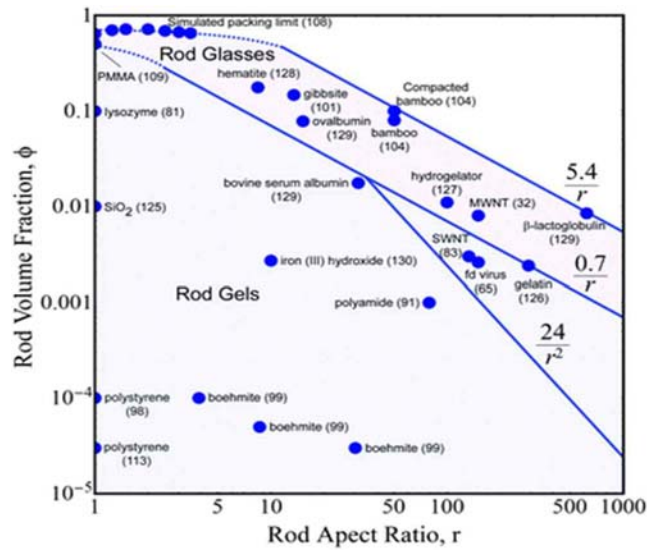


Figure 1.3 Map of the volume fraction and aspect ratio r dependences of rod gels and glasses. The figure is adapted from [5] with permission of The Royal Society of Chemistry (RSC).

Solomon et al. reviewed the phase behavior and rheological properties of rod-shaped colloids [5]. They argue that, depending on the strength of pair potential interactions, suspensions of rod-like particles form microstructures ranging from heterogeneous fractal clusters to homogeneous fiber networks. Further, they contend that the volume fraction range for transition between these two cases is strongly dependent upon rod aspect ratio. The two limiting microstructures can be distinguished by differences in structure factors in scattering experiments. Theories of the Brownian dynamics of fractal clusters and fiber networks show that these two types of microstructure can lead to the gelation and the glass transition, respectively (Figure 1.3). The dependence of the gelation/glass transition dynamics on volume fraction and aspect ratio for these two cases differ significantly. They reported that gels and glasses formation can be differentiated by probing this transition dynamics. The diffusivity of a rod in fiber networks at low volume fractions is orders of magnitude larger than that in fractal structure. Also the rod glass shows an abrupt down turn in the diffusivity with

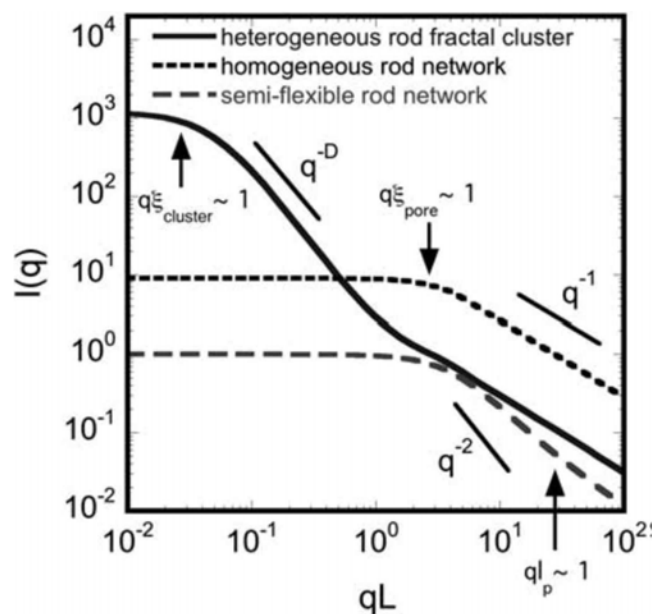


Figure 1.4. Comparison of the q -dependent scattering intensity, $I(q)$, for the limiting cases of rod suspension structure: homogeneous rigid rod networks and heterogeneous rod fractal clusters. The figure is adapted from [5] with permission of The Royal Society of Chemistry (RSC).

increasing volume fraction while the rod fractal gel shows a more gradual, power law type decrease. These different dynamics are the consequences of the difference in pair interactions: $U/kT \ll 1$ for glasses, while $U/kT \gg 1$ for gels.

1.3.3. Anisotropic particles flow behavior:

Under flow, suspensions of anisotropic particles exhibit many rheological properties qualitatively similar to those observed in concentrated spherical particle suspensions, such as reversible shear thinning and shear thickening, yielding behavior and thixotropy [3, 4, 39, 40]. Previously, Egres et al. explored the rheology and shear-induced microstructure of anisotropic particle suspensions through the shear thickening transition [4, 40]. For this investigation, acicular precipitated calcium carbonate (PCC) particles of varying particle aspect ratio ($L/D \sim 2, 4, 7$) dispersed in

poly(ethylene glycol) (PEG) are used demonstrate both continuous and discontinuous reversible shear thickening as a function of shear rate/stress. They found that the critical volume fraction for the onset of discontinuous shear thickening decreases as the average particle aspect ratio is increased. However, the critical stress for shear thickening is found to be independent of aspect ratio and volume fraction, and can be predicted based on the minor axis dimension of the particles in agreement with the critical stress scaling for hard-sphere suspensions. Small angle neutron scattering during shear flow (Rheo-SANS) demonstrates that long-axis particle alignment along the flow direction is maintained in shear thickening regimes for both continuous and discontinuous shear thickening PCC/PEG suspensions. The experimental results show that the critical volume fraction for discontinuous shear thickening can be associated with the concentration required for the equilibrium isotropic-nematic transition. The rheology and Rheo-SANS observations for the acicular PCC suggest that shear thickening in anisotropic particle suspensions is due to the short range hydrodynamic lubrication forces resulting in the formation of hydroclusters at high shear rates, analogous to the behavior in suspensions of spherical particles.

1.4 Objectives and Overview

The objective of this research is to understand the structure and rheology of gelling colloidal suspensions of anisotropic particles. This will be accomplished by extending the results previously reported for the gel transition and flow behavior of suspensions of adhesive hard spherical particles to suspensions of adhesive hard ellipsoidal particles. Comparing the responses of thermoreversibly gelling isotropic and anisotropic systems will provide quantitative evidence for the dependence of the gel transition and gel rheology on particle aspect ratio. As a first step, a well-characterized, dispersion of anisotropic particles having a uniform geometry and low polydispersity is synthesized as a model system. With this model system, the

connection between microstructure and bulk properties is established by means of rheology and SANS. The results are compared to studies by Eberle et al. [1, 8], who characterized the dynamical arrest and strength of attraction of model adhesive hard spheres comprised of thermoreversibly gelling octadecyl grafted silica nanoparticles in n-tetradecane. Next, the flow behavior of these model anisotropic particle suspensions has been investigated using rheo-SANS, which provides a means to understand the structure-property relationship under flow and to investigate the shear-induced microstructure of ellipsoidal particles under steady-shear flow.

Chapter 2

EXPERIMENTAL METHODS

2.1 Dynamic Light Scattering (DLS)

Dynamic light scattering is a technique that can be used to determine the size distribution profile of small particles in suspension or polymers in solution [41]. In this study, DLS is used to calculate the effective hydrodynamic particle diameter, D_H , from the diffusion coefficient measured from the decay of the autocorrelation of the scattered light from a particle in Brownian motion.

For measurements, the sample was sufficiently diluted to be visually clear such that the multiple scattering is minimized. The DLS measurements were performed on a Brookhaven Instruments Zeta PALS instrument, with a wavelength of 635 nm and a scattering angle at 90°. For each measurement, 10 runs for the duration of 2 minutes each were averaged together for sufficient statistics. We collect the Z -average diameter based on the average decay. As the model system in this study is non-spherical particles, a hydrodynamic equivalent diameter D_H (=diameter of a sphere with the same translational diffusion coefficient $D_{translation}$ as the particle in the same fluid under the same conditions), defined via the Stokes-Einstein relation.

$$D_H = \frac{kT}{3\pi\eta D_{translation}}. \quad (2.1)$$

where k is the Boltzmann constant, T the absolute temperature and η the viscosity of the liquid medium.

2.2 Transmission Electron Microscopy (TEM)

Transmission electron microscopy (TEM) is a microscopy technique in which electrons are transmitted through a specimen, and interact with the atoms in the

specimen as they pass through. In this study, TEM photomicrographs were obtained by using a JEOL JEM-2000FX instrument and Electron Microscopy Sciences 300C-CO grids. Small quantities of the dilute suspensions were dried at room temperature on TEM grids for overnight. The micrographs were analyzed using ImageJ [42] to determine long-axial (length), short-axial (diameter) dimensions and coating thickness of the model ellipsoid particles. Measurements of at least 100 particles from multiple micrographs were analyzed to ensure good statistical representation of mean particle dimensions and the polydispersity.

2.3 Rheometry

The suspensions were characterized using a DHR stress-controlled rheometer manufactured by TA Instruments. The tool geometry used was a 1° cone angle, 40 mm diameter. The sample was pre-sheared for 1 minute at 500s^{-1} before each measurement. In small amplitude oscillatory stress (SAOS) rheology, the experiments must be conducted in the linear viscoelastic (LVE) regime to accurately evaluate the relationships between material structure and viscoelastic behavior. Therefore, series of stress sweep measurements were performed to ensure that the applied stress is located with the linear LVE regime. After determining the appropriate stress corresponding to the linear regime, temperature sweep experiments at a frequency of 1 rad/s were conducted on the samples to probe the thermal effect on the sample viscoelasticity. The sample temperature was controlled by a Peltier plate to within 0.1°C . A temperature increment of 1°C and equilibrium time of 2 minutes at each temperature were used for both heating and cooling cycles. The frequency sweep measurements were then performed on the sample from 0.01 to 100 rad/s at a series of temperatures. For stress sweeps, we performed series of measurements ranged from 0.1 to 10 Pa in the ascending direction and 10 to 0.1 Pa in the descending direction.

2.4 Small-angle Neutron Scattering (SANS)

Small-angle neutron scattering (SANS) is a technique that uses an elastic neutron beam to probe the structure of nano-scale materials. Structural information is determined by analyzing the form factor and structure factor obtained from small angle neutron scattering. The form factor reveals single-particle properties such as particle size, geometric aspect ratio and polydispersity whereas structure factor, which can be obtained by Fourier transforming the radial distribution function, delivers the information of the interparticle displacement in the system such as the average particle-particle distance, phase information, and interparticle force such as attraction and repulsion.

The quantity measured in a neutron scattering experiment is an intensity distribution $I(q)$ for the scattering as a function of q . One approach to obtain the corresponding real-space structure is to express $I(q)$ by introducing the differential scattering cross section $d\sigma(q)/d\Omega$ which is in-dependent of the transmission and the form of the sample. In the case of randomly oriented, monodisperse scattering particles, the scattering cross section can be written as [43]

$$\frac{d\sigma(q)}{d\Omega} = n\Delta\rho VP(q)S(q) \quad (2.2)$$

where n is the number density of scattering particles, $\Delta\rho$ is the difference of the scattering length densities of the particles and the surrounding medium, V is the volume of the particle, $P(q)$ is the normalized ($P(q\rightarrow 0)=1$) form factor which describes the scattering from an individual particle, and $S(q)$ is the structure factor which describes the interference of neutrons scattered from different particles and is thus related to local correlations of different particles due to their interactions.

The normalized form factor ($P(q\rightarrow 0)=1$) is given by the product of the normalized

amplitude expression $f(q)$

$$P(q) = f(q)f^*(q) \quad (2.3)$$

where q is the scattering vector and defined by the difference of the wave vectors of the incident and scattered neutron beams. The normalized scattering amplitude of a homogeneous particle is given by the expression

$$f(q) = \frac{1}{V} \iiint_V e^{-iq \cdot r} dV \quad (2.4)$$

for the entire volume of the particle (V), or on the particle surface in the case that scattering occurs only from the particle surface. For a spheroid, $f(q)$ is known to be given as follows [44]

$$f(q, \alpha) = \frac{3(\sin(qr(a, b, \alpha)) - qr \cos(qr(a, b, \alpha)))}{(qr(a, b, \alpha))^3} \quad (2.5)$$

where α is the angle between the axis of the spheroid and the q -vector, a is the radius perpendicular to the rotation, b is the radius along the axis of the ellipsoid of the ellipsoid. Thus in the case of a prolate spheroid,

$$\frac{x^2}{a^2} + \frac{y^2}{a^2} + \frac{z^2}{b^2} = 1 \quad (2.6)$$

(major axis: b , minor axis: a) and the volume of the spheroid is

$$V = \frac{4\pi}{3} a^2 b \quad (2.7)$$

The average form factor can be obtained by the orientational averaging, thus:

$$P(q) = \langle f(q, \alpha)f^*(q, \alpha) \rangle = \frac{\int_0^\pi f(q, \alpha)f^*(q, \alpha) \sin \alpha d\alpha}{\int_0^\pi \sin \alpha d\alpha} = \frac{1}{2} \int_0^\pi f(q, \alpha)f^*(q, \alpha) \sin \alpha d\alpha \quad (2.8)$$

2.4.1. Static SANS

SANS experiments were performed on the NG7 30 m NIST SANS instrument. The suspensions were loaded into 1 mm path length demountable titanium cells, maintained at 25°C using the 10CB 10-position sample holder with a NESLAB circulating bath. It was assumed that the sample temperature was the same as the batch temperature. The wide range of scattering wavevector, Q , was obtained by combining the averaged scattering intensity from three different instrument configurations of 1m, 4m and 13 m detector distances (with focusing lenses at 13 m only). The wavelength of the neutron beam was 6Å with 10 – 15% wavelength polydispersity. SANS data reduction and analysis of the scattering intensity, I , versus Q was performed using the SANS reduction program in IGOR Pro, available from NIST [45].

2.4.2. Rheo SANS

Rheo-SANS was used to investigate the shear-induced structure in particulate suspensions under shear flow. The structure of a sample under flow can be probed in-situ while collecting the rheological response [46, 47]. The general experimental configuration for these techniques is provided in Figure 2.1, which illustrates the scattering spectra resulting from the neutron beam oriented in the radial and tangential direction.

The Couette cell consists of a cup-and-bob geometry and the fluid is maintained within the gap. Rheo-SANS experiments performed by using a 50mm ID quartz cup and 49 mm OD titanium bob such that the gap was 0.5 mm. A 2D cross-section of a Couette shear cell can be seen in Figure. 2.1. The Couette shear cell is driven by a controlled stress rheometer (Anton Paar MCR-501). For steady shear mode, the SANS measurements and the rheological measurements are synched each other. This offers the advantages of real time rheological measurement required for the investigation of shear-induced structure. Rheo-SANS experiments were performed on the NG-3 SANS instrument at the National Institute of Standards and Technology Center for Neutron Research (NCNR) in Gaithersburg, MD.

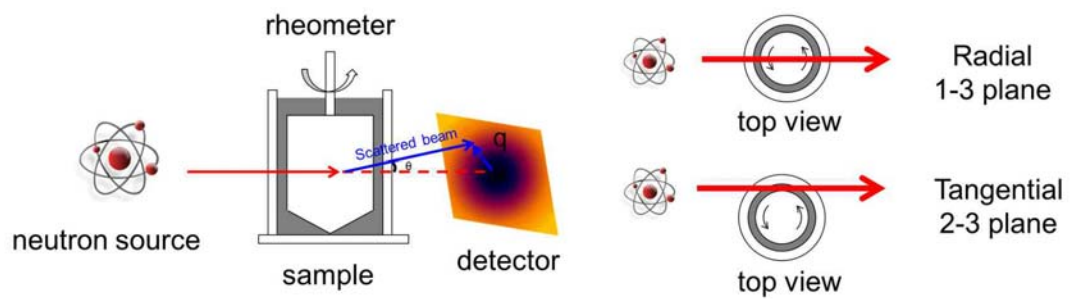


Figure 2.1. Rheo SANS shear cell configuration.

Chapter 3

THEORETICAL CALCULATION OF VAN DER WAALS FORCES FOR CORE-SHELL ELLIPSOIDAL PARTICLES

3.1 Orientation Dependent van der Waals Force

The sources of attractive forces that induce aggregation in this system are the attractive force from the thermally induced change of conformation of octadecanol brush in the solvent, which are desired, and the ubiquitous van der Waals forces acting between particles in solution. For silica particles, near refractive index matching insures that the latter forces are mitigated. However, anatase has a much higher refractive index than silica such that van der Waals forces acting between the titanium dioxide particle cores could lead to a temperature-independent attraction that could be sufficient to induce particle aggregation and thus, obfuscate the desired sol-gel transition. As a strategy to mitigate this van der Waals force, a silica coating is required in order to reduce the van der Waals forces between the TiO₂ cores by providing a steric barrier to keep them separated. This steric layer should be of sufficient thickness such that thermoreversible gelation arising from the interaction between the polymer brushes and n-tetradecane can be observed. Thus, the effect of silica coating thickness on the van der Waals attractions between the TiO₂ cores is investigated theoretically.

In the case of anisotropic particles the van der Waals force is dependent on the relative orientation between particles. To determine the appropriate steric barrier thickness it is necessary to identify the orientation of two anisotropic particles that has the strongest van der Waals attraction. For mathematical simplicity, the ellipsoids are assumed to be rod like particles. To account for the large curvatures at both ends, the Derjaguin Approximation [48] was used to relate the force law, $F(D)$, between two curved

surfaces to the interaction free energy per unit area, $W(D)$, between two planar surfaces. The Hamaker constant was obtained by using the following relations (3.1) and (3.2) while using the parameter values listed in Table 3.2.

Table 3.1 Equations of van der Waals energy between two rod-like particles in different geometries and corresponding spheres in terms of their Hamaker constant, A and surface to surface separation distance D .

| Particle orientation | van der Waals energy |
|-------------------------------|--|
| Faced | $\Phi_{vdw} = -\frac{A}{12\pi} \left(\frac{1}{D^2} + \frac{1}{(D+L_1+L_2)^2} - \frac{1}{(D+L_1)^2} - \frac{1}{(D+L_2)^2} \right)$ |
| Sphere | $\Phi_{vdw} = -\frac{A}{6D} \frac{R_1 R_2}{(R_1 + R_2)}$ |
| Crossed | $\Phi_{vdw} = -\frac{A\sqrt{R_1 R_2}}{6D}$ |
| Parallel (per unit length) | $\Phi_{vdw} = -\frac{AL}{12\sqrt{2}D^{3/2}} \left(\frac{R_1 R_2}{(R_1 + R_2)} \right)^{1/2}$ |

$$A_{11} = \frac{3}{4} kT \left(\frac{\varepsilon_1 - \varepsilon_3}{\varepsilon_1 + \varepsilon_3} \right)^2 + \frac{3h\nu_e}{16\sqrt{2}} \frac{(n_1^2 - n_3^2)^2}{(n_1^2 + n_3^2)^{3/2}}, \quad (3.1)$$

$$A_{132} = \frac{3}{4} kT \left(\frac{\varepsilon_1 - \varepsilon_3}{\varepsilon_1 + \varepsilon_3} \right) \left(\frac{\varepsilon_2 - \varepsilon_3}{\varepsilon_2 + \varepsilon_3} \right) + \frac{3h\nu_e}{8\sqrt{2}} \frac{(n_1^2 - n_3^2)(n_2^2 - n_3^2)}{(n_1^2 + n_3^2)^{1/2} (n_2^2 + n_3^2)^{1/2} \left\{ (n_1^2 + n_3^2)^{1/2} + (n_2^2 + n_3^2)^{1/2} \right\}} \quad (3.2)$$

As shown in Figure 3.1, the van der Waals force between two parallel rods is the greatest among the various orientations. This force is significantly greater than that obtained between two spheres of corresponding volume, which indicates that such a spherical particle assumption would lead to erroneous calculations of particle stability.

Therefore, we consider a parallel orientation to calculate the optimum silica coating thickness in following section.

Table 3.2 Parameters used for the calculations of van der Waals energy

| Parameter | Definition | Value | Source |
|--------------|---------------------------|---|-----------------------------------|
| k | Boltzmann constant | $1.381 \times 10^{-23} \text{ J} \cdot \text{K}^{-1}$ | [55] |
| T | temperature | 20°C | arbitrary experimental conditions |
| ϵ_1 | dielectric constant of 1 | 86 | [55] |
| ϵ_2 | dielectric constant of 2 | 4.42 | [55] |
| ϵ_3 | dielectric constant of 3 | 2.03 | [55] |
| h | Planck constant | $6.626 \times 10^{-34} \text{ J} \cdot \text{s}$ | [55] |
| ν_e | UV frequency | $3 \times 10^{15} \text{ s}^{-1}$ | - |
| n_1 | refractive index of 1 | 2.61 | [55] |
| n_2 | refractive index of 2 | 1.5442 | calculated |
| n_3 | refractive index of 3 | 1.418 | [55] |
| A_{11} | Hamaker constant of 1-1 | $2.35 \times 10^{-19} \text{ J}$ | calculated |
| A_{22} | Hamaker constant of 2-2 | $4.449 \times 10^{-21} \text{ J}$ | calculated |
| A_{33} | Hamaker constant of 3-3 | 0 | calculated |
| A_{132} | Hamaker constant of 1-3-2 | $3.11 \times 10^{-20} \text{ J}$ | calculated |

*1 is TiO_2 , 2 is SiO_2 , and 3 is tetradecane

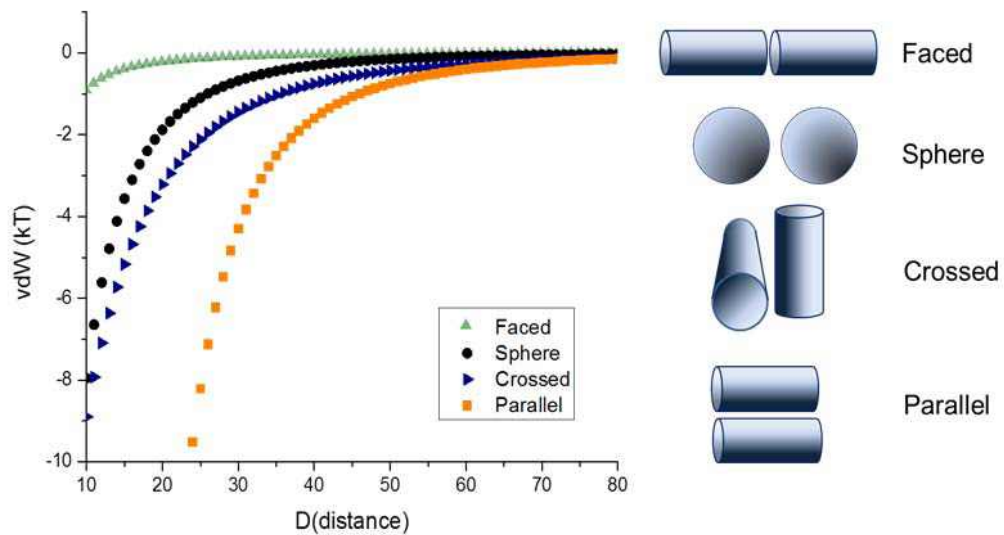


Figure 3.1 Orientation-dependent van der Waals interactions of two rod-like particles of aspect ratio 4.78 as a function of surface to surface separation distance (nm). The values are also given for corresponding spheres ($r=32\text{nm}$) of equivalent volume.

3.2. Calculation of van der Waals Force of Core-shell Ellipsoid

A method for calculating the van der Waals interactions between core-shell spherical particles was published by Viravathana et al. [49] and corrected by Kim (PhD Thesis, UD). By assuming pairwise additivity of the system, the core-shell system can be decomposed into several different components. Figure 3.2 suggests the individual components where (a), (b) and (c), and (d) represent a core-core, core-shell, and shell-shell interaction, respectively. After decomposition, all the components can be expressed as a sum and difference of various pure core or shell material.

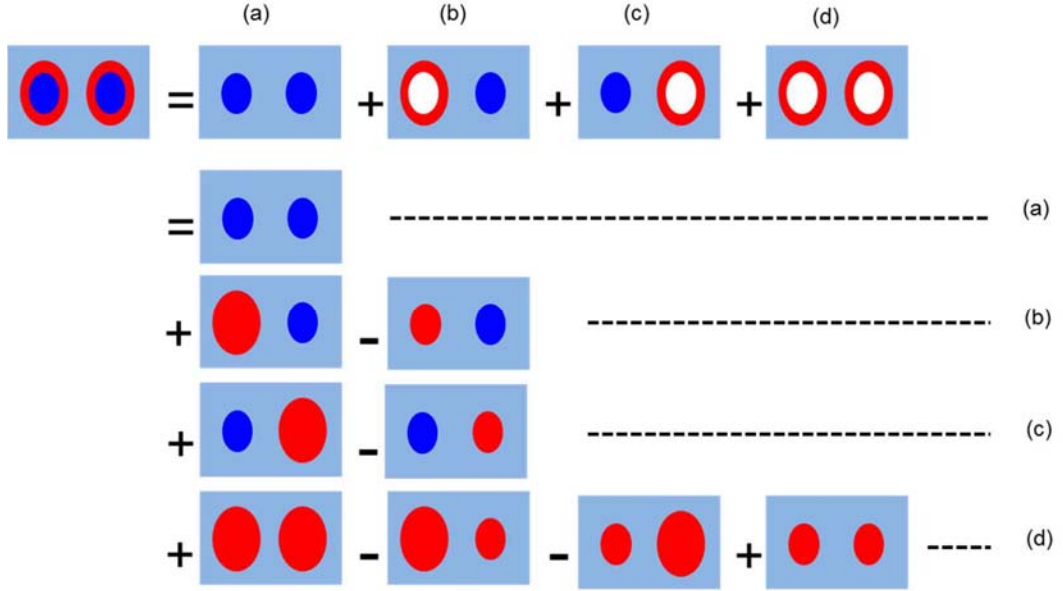


Figure 3.2 Individual components of the van der Waals interactions of a core-shell ellipsoids in parallel orientation. Image courtesy of Jung Min Kim.

The van der Waals energy between two colloidal particles of 1 and 2 can be obtained by the following equation [48]:

$$\Phi = -\frac{A_H}{\pi^2} \int_{V_1} \int_{V_2} \frac{d\mathbf{x}_1 d\mathbf{x}_2}{r^6} \quad (3.3)$$

where $r^2 = (\mathbf{x}_1 - \mathbf{x}_2) \cdot (\mathbf{x}_1 - \mathbf{x}_2)$, \mathbf{x}_i : coordinate in particle i and A_H is Hamaker constant. This is a multiple integral of 6th order because $d\mathbf{x}_1$ and $d\mathbf{x}_2$ represent volume elements. The van der Waals energy between two parallel ellipsoids of different sizes can be obtained by the following method: We consider the prolate spheroidal coordinates (η , θ , ϕ) [50]

$$\begin{aligned} u^1 &= \eta, & 0 \leq \eta < \infty \\ u^2 &= \theta, & 0 \leq \theta \leq \pi \\ u^3 &= \phi, & 0 \leq \phi \leq 2\pi \end{aligned} \quad (3.4)$$

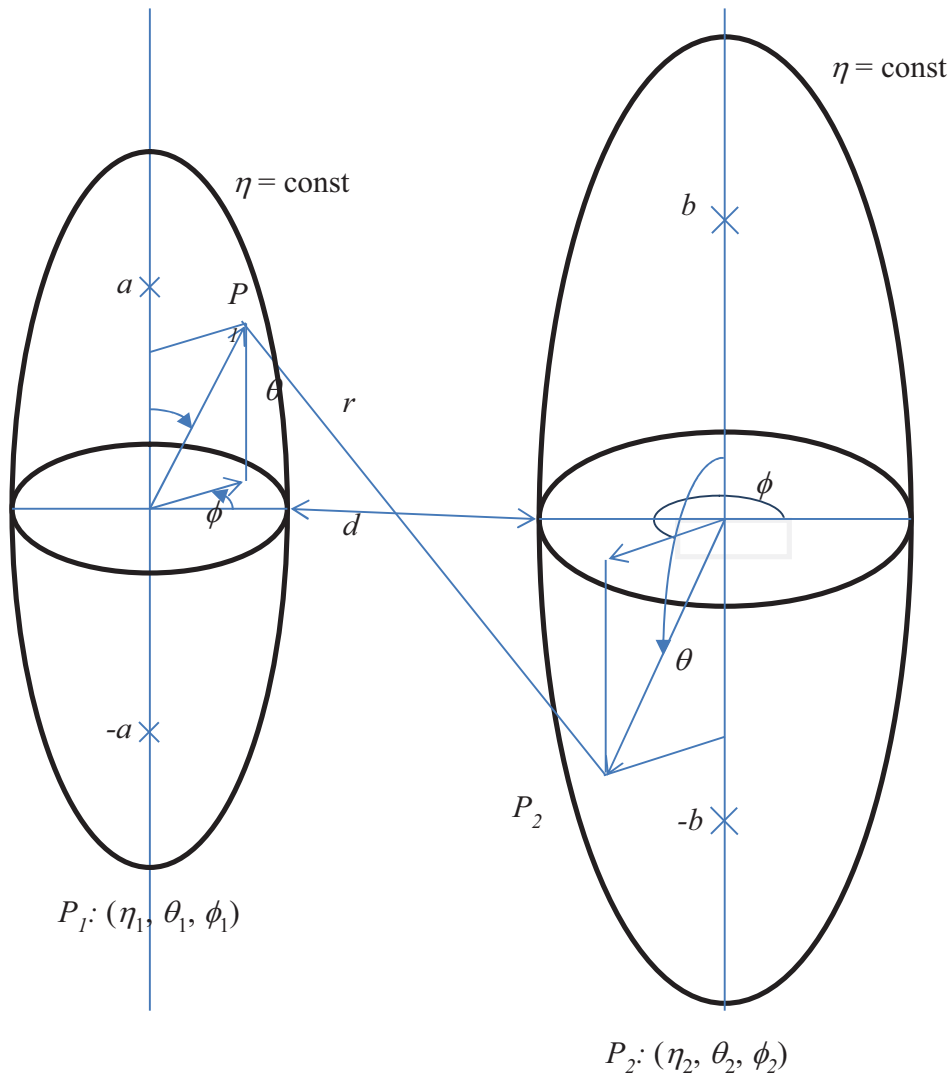


Figure 3.3 Geometry of ellipsoids with different radius in prolate spheroidal coordinates

The prolate spheroidal coordinates and the Cartesian coordinates are related with the following relationship,

$$\begin{aligned}
 x &= a \sinh \eta \sin \theta \cos \phi \\
 y &= a \sinh \eta \sin \theta \sin \phi \\
 z &= a \cosh \eta \cos \theta
 \end{aligned}
 \tag{3.5}$$

And a prolate spheroid surface is expressed by the following equation:

$$\frac{x^2}{a^2 \sinh^2 \eta} + \frac{y^2}{a^2 \sinh^2 \eta} + \frac{z^2}{a^2 \cosh^2 \eta} = 1 \quad (3.6)$$

The foci of the spheroid are located at $y = \pm a$ and the lengths of the major and minor axes are $a \cosh \eta$ and $a \sinh \eta$, respectively. A constant corresponds to the surface of the ellipsoids. Now we consider two ellipsoids. The center of the first ellipsoid is located at the origin, the foci are at $y = \pm a$ and the surface is represented by Eqn. (3.6) with $\eta = A$. The center of the second ellipsoid is located at $x = a \sinh A + b \sinh B + d = L$, the foci are at $y = \pm b$ and the surface is represented by Eqn. (3.6) with $\eta = B$. Then the shortest distance between two ellipsoids is d . Then the distance r between two points P_1 and P_2 is thus:

$$r^2 = (x_2 - x_1 + L)^2 + (y_2 - y_1)^2 + (z_2 - z_1)^2 \quad (3.7)$$

where

$$\begin{aligned} x_2 - x_1 &= a(\sinh \eta_2 \sin \theta_2 \cos \phi_2 - \sinh \eta_1 \sin \theta_1 \cos \phi_1) \\ y_2 - y_1 &= a(\sinh \eta_2 \sin \theta_2 \sin \phi_2 - \sinh \eta_1 \sin \theta_1 \sin \phi_1) \\ z_2 - z_1 &= a(\cosh \eta_2 \cos \theta_2 - \sinh \eta_1 \cos \theta_1) \end{aligned} \quad (3.8)$$

And the volume elements are

$$\begin{aligned} dV_1 &= a^3 (\sinh^2 \eta_1 + \sin^2 \theta_1) \sinh \eta_1 \sin \theta_1 \\ dV_2 &= a^3 (\sinh^2 \eta_2 + \sin^2 \theta_2) \sinh \eta_2 \sin \theta_2 \end{aligned} \quad (3.9)$$

Then the shape factor S (without the Hamaker constant) is given as follows:

$$-\frac{1}{\pi^2} \int_0^B \int_0^\pi \int_0^{2\pi} \int_0^A \int_0^\pi \int_0^{2\pi} \frac{dV_1 dV_2}{r^6} \quad (3.10)$$

In the present research, the sizes of the major and minor axes of TiO₂ core are 182nm and 38nm, respectively. Assuming that the coating thickness of silica shell is uniform, we can obtain b and B . The numerical integration was carried out while varying the thickness of the shell and the distance between two ellipsoids, d .

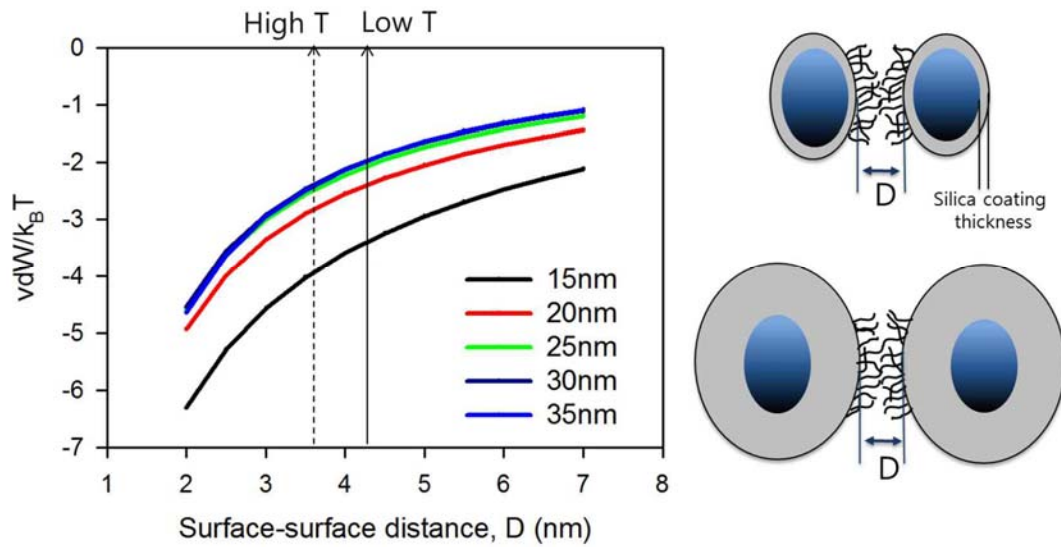


Figure 3.4 van der Waals interactions of core-shell spherical silica-coated TiO₂ with different silica shell thickness. Solid and dotted lines correspond to surface-surface distance taking into account octadecyl brush height at low temperature and high temperature, respectively.

In the course of calculations, we obtained the van der Waals energies between TiO₂-TiO₂, TiO₂-SiO₂ and SiO₂- SiO₂ pairs of small-small, small-large and large-large sizes using the corresponding Hamaker constant using Eqns (3.1) and (3.2) with parameter values listed in Table 2. Here the size of TiO₂ particles is denoted by small and the size of the silica shell is denoted by large. Then the values were added or subtracted as obtained for spherical core-shell structures. Figure 3.4 shows the change in van der Waals energy as a function of the separation between two ellipsoids for several silica coating thicknesses. The van der Waals energy increases when the coating thickness increases from 15nm to 25nm (The absolute values decrease in this cases). Then the

energy decreases slightly as the thickness increases further. The increase of van der Waals energy up to coating thickness of 30nm is due to the shielding effect of silica. Therefore the coating thickness of the TiO₂ particles is chosen to be 30nm. At this thickness, the van der Waals forces between touching particles in parallel orientation is calculated to be ~ -2 kT, which is still significant but amenable to thermal fluctuations such that only weak flocculation would be expected. These calculations also demonstrate that additional silica coating will not improve stability. Note that additional coating also reduces the particle aspect ratio and increase the particle size (and mass), such that it is undesirable.

Chapter 4

PARTICLE SYNTHESIS AND CHARACTERIZATION

4.1 Particle Synthesis

Model Adhesive hard ellipsoid particles (denoted AHE) consisting of titanium dioxide particles as the core [51] coated with a silica shell [52] have been synthesized. The silica coating layer has been specifically designed to produce the same surface chemistry as previously-studied adhesive hard spheres [6, 7] and to reduce the strong van der Waals attraction between TiO_2 core particles. Octadecyl chains are grafted onto the silica surface so that the system exhibits a thermoreversible gelation [17, 19, 20, 23, 53]. The following procedure is used for each step:

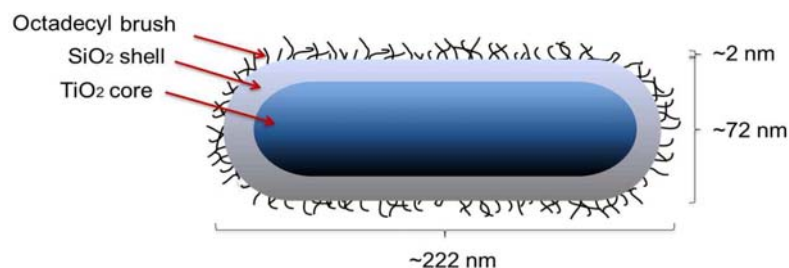


Figure 4.1 A schematic of the model anisotropic particle consisted of ellipsoidal TiO_2 particle as the core coated with a silica shell with octadecyl chain grafting on the surface (not to scale). The particle geometry is idealized as a sphereocylinder for purposes of showing the particle's layered structure.

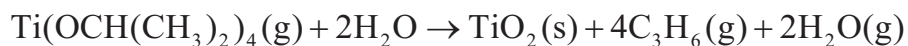
4.1.1 Synthesis of ellipsoidal TiO_2 particles

In this project, we synthesize TiO_2 ellipsoids as the starting cores for the reproducible preparation of well-defined, monodisperse ellipsoids. The synthesis protocol follows that of Sugimoto et al. [51] with minor modification. Ellipsoidal anatase (a crystalline

form of titanium dioxide) was synthesized based on a two-step sol-gel method for the titanium (IV) isopropoxide (Fisher, 99 wt %) and triethanolamine (TEOA) (Fisher, 98 wt%) mixture, with TEOA. This facilitates the formation of the ellipsoidal shape over the usual cuboidal titania morphology through growth rate reduction of specific crystal planes at a pH above 11.

As a first step, TIPO and TEOA with a molar ratio of [TIPO : TEOA] = [1:2] were first thoroughly mixed and then diluted with Milli-Q water to obtain a stable complex of 0.5M Ti⁴⁺. Initially TIPO was added to the flask then TEOA and the mixture was stirred for 10 mins, then water was added to get TIPO = 2M and the aqueous solution stirred for another 10 mins before adding the 2M ammonia hydroxide solution. The whole mixture was stirred for an additional 10mins, resulting in a final solution pH of 11. The mixture of TIPO/TEOA/H₂O/NH₄OH was transferred in 800 ml quantities to 1L pressure resistant Pyrex pressure bottles (Ace Glass, Cat# 5557-20) with Teflon lined screw caps (Fisher Scientific, Cat#064142C). Both bottles and caps have high temperature resistance (140°C). The solution was aged at 100 °C for 24 h, and further aged at 140 °C for 72 h. The first aging step generates a hydrolyzed translucent gel whereas the second aging step initiates the nucleation and growth of the particles. The gel matrix plays an important role as it serves to control the nucleation rate by lowering the super-saturation of the metal ions as well as the growing rate of the particles [4]. Following the reaction temperature cycle, the bottles were allowed to cool to room temperature and TiO₂ particles and mother liquor were separated from the residual gel matrix through filtration using a funnel lined with glass wool. The filtered suspension was centrifuged at 16,000 g for 2 h. The resulting sediment was re-dispersed in water and centrifuged again. The redispersion/centrifugation steps were repeated twice to remove residual organic compounds from the surface of the nanoparticles

The theoretical yield can be calculated from the main chemical reaction according to the reaction given as [54]:



Thus for each mole of TIPO used, one mole of TiO_2 is produced, although other side reactions occur [54]. Therefore the theoretical mass can be calculated as:

$$\begin{aligned} \text{Mass}(\text{TiO}_2) &= n(\text{TiO}_2) \times \text{Mw}(\text{TiO}_2) \quad \text{where} \\ n(\text{TiO}_2) &= \text{mass of pure (TIPO)} / \text{Mw}(\text{TIPO}) \\ \text{mass of pure (TIPO)} &= \text{wt \%} \times \text{mass of TIPO solution} / 100 \end{aligned}$$

Thus for 293.20 gm of TIPO solution (or 1 mole of pure TIPO), and a molar mass of 79.866 g/mol for TiO_2 , the theoretical yield is about 79.87 gm.

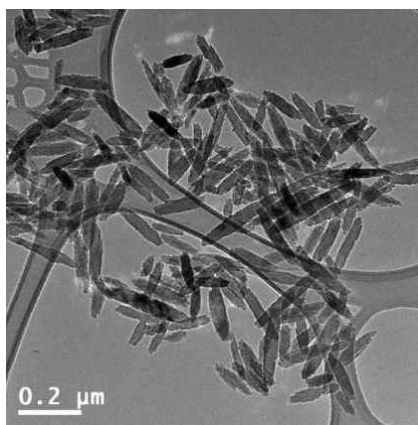


Figure 4.2 Transmission electron micrograph of ellipsoidal TiO_2 particles synthesized through gel-sol synthesis

Table 4.1 Properties of ellipsoidal TiO₂ core particle

| | |
|--------------------------|-------------|
| Particle length (nm) | 182 ± 19 |
| Particle diameter (nm) | 38 ± 2 |
| Particle aspect ratio | 4.78 ± 0.56 |
| Effective diameter (DLS) | 165.6 ± 13 |

4.1.2 Silica coating

The synthesis protocol of Sacanna et al. [52] was followed to create a silica coating on the anatase ellipsoids with some modification to optimize the procedure. Uniform silica-coated TiO₂ particles can be obtained when the seed concentration in the reaction mixture does not exceed 0.5 g/L. Further, the reaction must be carried out under continuous ultrasonication to avoid the formation of clusters during the silica growth. Before adding tetraethyl orthosilicate (TEOS), poly(vinylpyrrolidone) (PVP) with average molar mass of 45 kg/mol (Sigma-Aldrich) was adsorbed onto the TiO₂ particles to hinder particle aggregation, such that uniform silica-shell growth can be carried out. Prior to adsorption reaction, 7.9 g of PVP was dissolved in 200mL of ethanol by magnetic stirrer. Then 0.5 g of TiO₂ in 3.65 mL MilliQ water was added into the PVP solution, and the mixture was kept under stirring for 24 h. To remove unabsorbed PVP molecules, the dispersion was centrifuged for 3 h at 5000g using a Beckman and Coulter XP-L100 ultracentrifuge. After the centrifugation, the supernatant was discarded and the sediment was redispersed into 75 mL of ethanol.

In this silica coating step, 59 mL of MilliQ water, 15 mL of TMAH (1%v/v aqueous solution), and 80g of PVP-stabilized TiO₂ dispersion (0.63 wt %) were added to 655 mL of ethanol in a 2 L reaction bottle under ultrasonication. Then a mixture of 4 mL of TEOS and 2mL of ethanol was added under the surface of the reaction mixture in three portions every 20 min. The addition of TEOS was continued until the total TEOS

volume of 16 mL. After the last addition, the dispersion was kept under ultrasonication and stirring for at least 3 h. Silica coated TiO₂ particles were centrifuged at 5000 g for 2 hours, and the sediments were redispersed in ethanol.

The silica coating thickness based on the geometry in Figure 4.1 assuming 100% yield of TEOS hydrolysis can be calculated by using the equation below derived from a mass balance:

$$d_{thickness} = \left[\frac{1}{\pi(2\alpha - 2/3)} \left((2\alpha - 2/3)r^3 + \frac{[TEOS]Mw_{SiO_2}V_{solution}}{\rho_{SiO_2}N} \right) \right]^{1/3} - r \quad (4.1)$$

where d is the silica coating thickness, $V_{solution}$ is the total volume of the solution, Mw_{SiO_2} is the molecular weight of silica, r is the minor radius, N is number of particles, α is aspect ratio, and ρ_{SiO_2} is the density of silica. Calculations were performed using a density of silica of 2.6g/cm³, obtained from [55]. Comparing the calculation with the measurement gives that the hydrolysis of TEOS on core particles has 60.7% yields when we follow the current coating protocol as described above. Calculations of the required coating size of 30 nm as presented in Chapter 3 were used to select the coating thickness used for the remainder of this work.

4.1.3 Effect of PVP molecular mass

One of the most critical steps in this silica coating procedure is transferring TiO₂ particles that are charged and stable in aqueous solution to ethanol, where the Stöber process is performed. The anatase particles were not sufficiently stable in ethanol without modification. To achieve the transfer and maintain sufficient stability, TiO₂ particles are coated with an adsorbed layer of poly (vinylpyrrolidone) (PVP) in aqueous solution [56]. If the particles are then sufficiently stabilized, they can be

transferred into ethanol and be further coated with a silica layer using the Stöber method. In this section, we demonstrate that the molar mass of the PVP used plays a crucial role in the stability of the particles during the growth process.

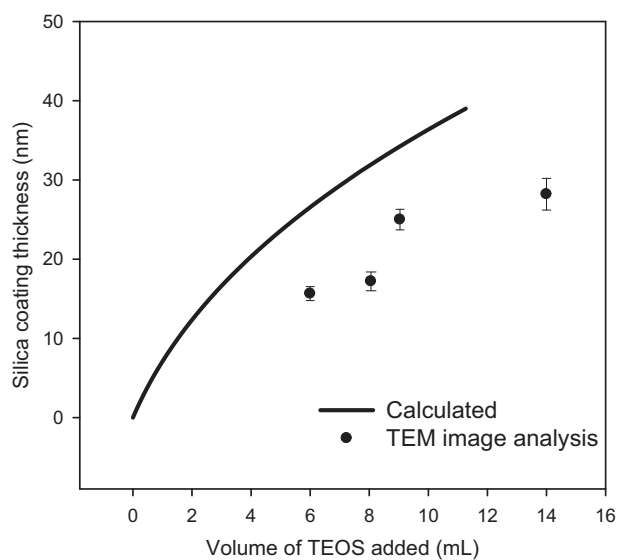


Figure 4.3 Effect of TEOS addition for the silica-coating process on mean particle diameter, as measured from TEM images and calculated theoretically.

Tetraethyl orthosilicate (TEOS>99%) was obtained from Fisher Scientific. poly(vinylpyrrolidone) with average molar masses of 54kg/mol(PVP-54k) and of 10kg/mol(PVP-10k) was purchased from Sigma-Aldrich. Ethanol (>99%) was purchased from Fisher Scientific. MilliQ water with resistivity 18.2 MΩcm was used. First, PVP was dissolved in ethanol and 0.5g of TiO₂ was added in the solution and then stirred for 24h. After the adsorption, the particles are separated from ethanol by centrifugation at 5000g for 2 hours. Next, the supernatant was removed and the particles were redispersed in ethanol. This solution could be directly used in the silica coating step

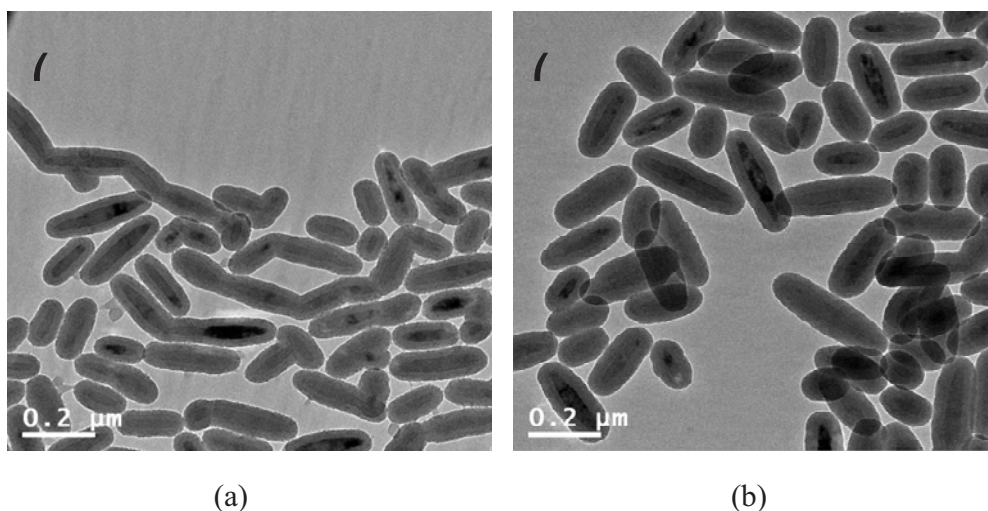


Figure 4.4 TEM micrographs of TiO₂ coated with silica after coated with PVP-54k (a) and PVP-10k (b)

The comparison of Figure 4.4(a) and Figure 4.4(b) shows a influence of the length of the polymer used: while the particles coated with PVP-10k are nearly uniform and disperse as individual particles (Figure4.4(b)), the particles coated with PVP-54k show many fused particles (Figure4.4(a)). It is very evident in the micrographs that many particles are aggregated end-to-end. Thus, counterintuitively, the lower molar mass PVP is observed to be more effective in stabilizing the particles during coating. A possible explanation is found in the observation that for the larger polymer (PVP-54k), sometimes particles appear to be only partially coated with silica during synthesis. Thus, in this case the particles are not sufficiently stabilized during the conditions of the Stöber growth and grow together with other particles. It is hypothesized that polymer coverage at the highly curved particle ends is not sufficient to prevent end-to-end aggregation during coating, which leads to end-to-end fusion. There should be an optimum PVP molecular mass for a given size and curvature of particles, such that it is large enough to provide sufficient steric stabilization of the particles to avoid aggregation during the silica shell growth, but small enough to cover the whole surface of particle [57]. In present study, we use PVP-10k to stabilize TiO₂ particles.

We verify that the length of the polymer used strongly influences the stability of the colloids and the uniformity of the silica coating.

4.1.4 Octadecyl polymer brush grafting onto SiO₂-TiO₂ surface

The last step of synthesis is grafting octadecyl polymer brushes on the silica surface, which allows thermally controlling attractive force between particles dispersed in n-tetradecane. When the particles are dispersed in a medium of linear hydrocarbon chains such as n-tetradecane, the two-component system consisting of the particles and the solvent exhibits a short-range attraction and undergoes a thermoreversible first-order phase transition between solid and liquid within a narrow change of temperature [15, 17, 18, 58, 59]. The strength of attraction is controlled by thermal quenching and the range of attraction is usually characterized by the thickness of the chain layer. Here the polymer brush should be short enough to assume that the coatings on the particles are uniform.

Adhesive hard ellipsoids (AHE) were prepared by grafting 1-octadecanol (C₁₈H₃₇OH, 99+%, Alfa Aesar) onto the surface of ellipsoidal SiO₂ coated particles by an esterification process following the established protocol [23] as follows: First, 20 g of the particle suspension was mixed with 62.5 g of ethanol and 60g of 1-octadecanol with 2 drops of sulfuric acid and followed by an addition of 200 g of ethanol. The mixture of 1-octadecanol-silica-ethanol was slowly heated to the reaction temperature using a rotary evaporator (RE211 from Buchi) immersed in an oil bath with a temperature control. The reaction flask was immersed in the oil bath and heated to 70 °C and equilibrated for 15 minutes. Then the temperature was raised by 10°C every 15 minutes. Finally, the temperature was increased to 230°C and the reaction was allowed to proceed for 5 hours. After the mixture was cooled to room temperature, the remained cake was dissolved in a mixture of chloroform and cyclohexane (3:2 vol/vol)

and the particles were redispersed by removing excess 1-octadecanol.

To prepare dispersions of the model ellipsoidal particles in n-tetradecane, a concentrated dispersion of the particles in cyclohexane was transferred to a vial and the cyclohexane was evaporated under a nitrogen stream for 2 hours at room temperature. The remaining cyclohexane evaporated in a vacuum oven at -30 inHg for overnight. After addition of n-tetradecane, the sample was placed in an oven at 50°C for 4 days and vortex-mixed every 6 hours at 3000 RPM to disperse the particles. The well dispersed sample was fluidized in room temperature.

4.2 Particle Characterization

4.2.1 Particle geometry (TEM)

Transmission electron microscopy (TEM) (JEOL JEM-2000FX at 200 kV) was used to characterize the particle size and shape. The analysis of the TEM images was carried out with ImageJ [42] by measuring at least 100 particles. TEM analysis gave the average diameters of 210 ± 32 nm and 84 ± 3 nm for the major and minor axes, respectively, which yields an aspect ratio of 2.5 ± 0.4 with silica coating thickness of 33 ± 1 nm. In TEM micrograph, we found there are approximately 2 to 4 doublets out of 100 particles and few aggregates are observed. No filtering was carried out for sample preparation.

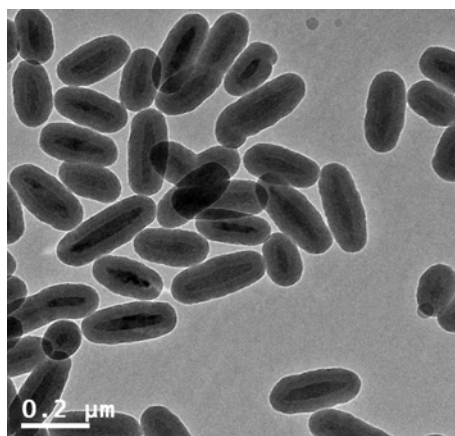


Figure 4.5 Transmission electron microscope images of SiO₂-TiO₂ particles

Table 4.2 Properties of Adhesive hard ellipsoid particles

| | |
|---|---------------|
| Particle length (nm) | 210 ± 32 |
| Particle diameter (nm) | 84 ± 3 |
| Particle aspect ratio | 2.5 ± 0.4 |
| Coating thickness (nm) | 33 ± 1 |
| Rotational diffusivity (s ⁻¹) | 222 |

DLS measurements were carried out for bare particles only. It was assumed that the octadecyl grafted particles have the same dimensions because the brush size is even smaller than the experimental error of the DLS method. The suspension of ellipsoid particles in n-tetradecane was turbid and the viscosity of the suspension of ellipsoid particles appears not to be increased much from pure tetradecane. No sedimentation was observed when placed on a shelf overnight.

4.2.2 Characterization by SANS

SANS experiments on very dilute suspensions of TiO₂ particles dispersed in D₂O were

performed on the NG7 30 m SANS instrument. SANS data reduction to obtain the scattering intensity, I , versus Q was performed using the SANS reduction program in IGOR and the analysis to obtain the particle characteristics was done with SASView, which had polydispersity included for ellipsoids. From the results, the particles are 116 ± 5.2 nm in length and 18.2 ± 0.032 , resulting into an aspect ratio of 6.4.

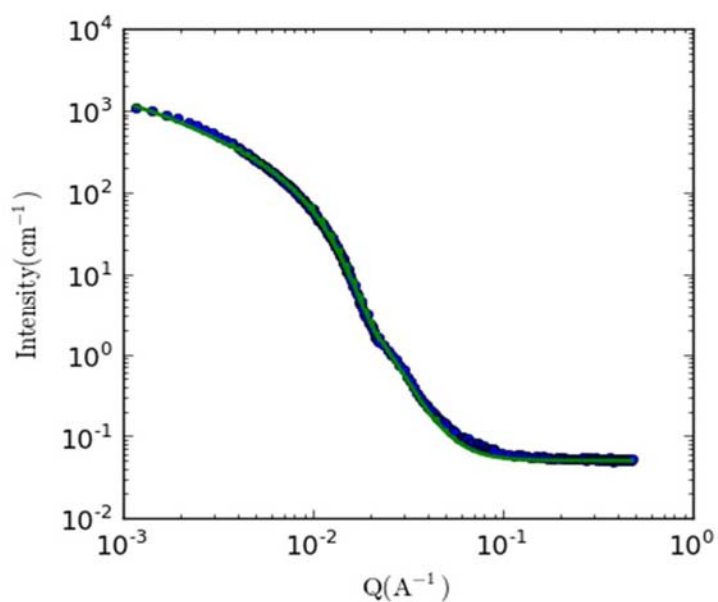


Figure 4.6 Intensity vs. scattering vector for bare TiO₂ in D₂O. Green line is the fitted curve.

Table 4.3 SANS modeling for bare TiO₂ in D₂O.

| | |
|------------|--|
| background | 0.05 [1/cm] |
| radius_a | 116 ± 5.2 [nm] |
| radius_b | 18.2 ± 0.32 [nm] |
| scale | $0.0030101 \pm 2.8 \times 10^{-6}$ |
| sldSolv | 6.33×10^{-6} [1/ Å ²] |

The packing characteristics of the spheroids can be predicted by the Monte Carlo simulations by Frenkel and Mulder [32]. Their calculation for hard ellipsoids of revolution shows that the aspect ratio of 2.5 is not sufficient to form a nematic phase (The minimum aspect ratio for the nematic transition reads approximately 10 in their plot.) and particles undergo a solid phase transition at a volume fraction of around 11.8%. The percolation threshold for hard ellipsoids was reported by Garboczi et al. [6]. When aspect ratio is 2.5, the threshold is obtained to be 24.5% by the cubic fit to their tabulated data. This value is slightly smaller than the value for spheres of 28.54%. This shows that weak attractions are operative if we can form a weak gel with a weak yield stress at 6 vol %, consistent with our observations. The phase behavior of the rodlike particles has been reported for the Gay-Berne model of attractive ellipsoids of aspect ratio of 3 by Miguel et al. [60]. Because the potential ratio between two parallel and two axially positioned particles has not been quantified for the present system and the aspect ratio is not the same, the direct comparison may not be possible. However the critical volume fraction they obtained for their system is 19.6%. This value is far larger than the volume fraction of 6% we consider here and hence no condensation is expected to occur in our case.

Chapter 5

RHEOLOGICAL RESULTS AND DISCUSSION

In this chapter, the rheologically defined gel temperatures are found and compared with corresponding spherical systems. The gel temperatures are determined by performing a series of small amplitude oscillatory measurements with varying frequency across a range of temperatures.

In this system, the nature of the gels is physical gels, which means, it has reversible bonds. Compared to a chemical gel, which is an irreversible gel formed with bonds of infinite relaxation time, a particulate physical gel has interparticle bonds with finite energy and lifetimes and therefore, we can observe reversible gelation [3]. This also means that any physical gel will eventually creep and flow if observed over a sufficiently long timescale. Because gelation is a type of dynamical arrest that will depend on the observation time and method, a rigorous scientific definition of critical gelation is necessary rather than just identifying dynamical arrest in a specific experiment. It has been demonstrated that the rigorous definition of critical gelation can be applied to characterize physical gelation using a rheological method [1]. Winter and Chambon demonstrated a gelation criterion using the frequency dependence of the sample's linear viscoelastic behavior. At the critical gel point, both the storage modulus (G') and loss modulus (G'') show power-law dependence with the same exponent across a broad range of frequencies [2, 61]. Due to the physical nature of the gel, this frequency dependence will always turn over to terminal fluid behavior at sufficiently low frequencies, although beyond the critical gel point this frequency can be so low as to be immeasurable.

5.1 Preshear

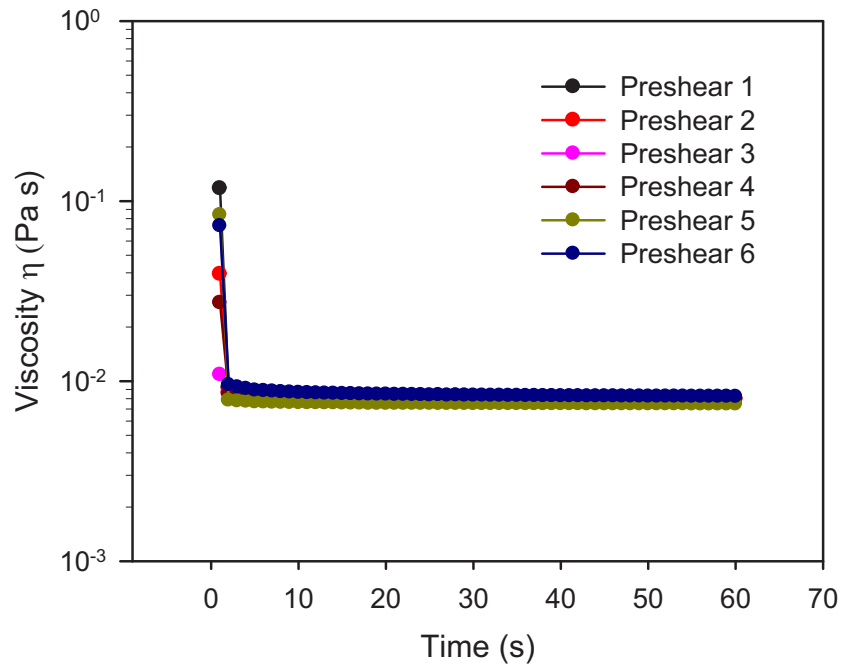


Figure 5.1 Suspension viscosity during preshearing at 500s^{-1} for 60 seconds at the beginning and between measurements. All measurements performed at $20\text{ }^{\circ}\text{C}$.

As noted in the methods section, the rheological characterization was performed on a stress-controlled rheometer (DHR, TA Instruments) with a cone-plate geometry (1° cone angle, 40 mm diameter). A preshear is applied to check whether particles sediment during the duration of the experiment and to establish a consistent microstructure before the tests. Prior to performing each experiment, a preshear at 500s^{-1} for 60s was conducted at $20\text{ }^{\circ}\text{C}$. As seen in Figure 5.1, within 5 seconds the viscosities measured during preshears conducted at various points within a sequence of tests overlap each other. If the viscosities during the preshear did not reach the same values the tests were terminated and a fresh sample was loaded.

5.2 Temperature Sweep

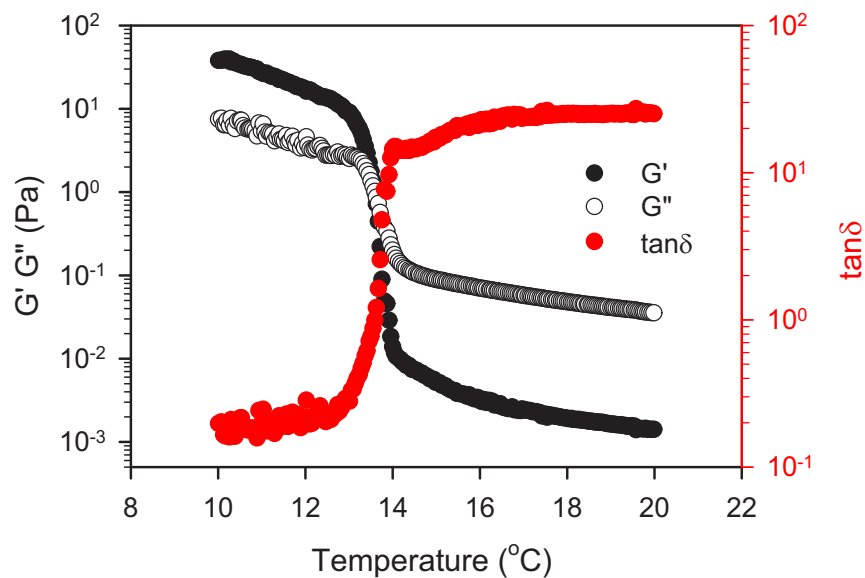


Figure 5.2 Temperature ramp measurement of 6 vol% AHE suspension at an oscillatory frequency of 1 rad/s and temperature ramp rate of 0.2°C/min.

The rheological characterization was performed on a stress-controlled rheometer (DHR, TA Instruments) with a cone-plate geometry (1° cone angle, 40 mm diameter) with a Peltier temperature controller at temperatures ranging from 10°C to 20°C. At a constant frequency of 1 rad/s, a series of increasing oscillatory amplitude measurements was performed on 6 vol% AHE suspension to determine the extent of the linear viscoelastic regime in order to ensure that the equilibrium microstructure was probed. After determining the appropriate oscillatory amplitude corresponding to the linear regime, temperature sweep experiments at a frequency of 1 rad/s were performed. A temperature ramp rate of 0.2°C/min was used for both heating and cooling cycles.

Figure 5.2 shows storage and loss moduli (G' and G'') as a function of temperature from the heating cycles on 6 vol% AHE suspension. Figure 5.3 shows the change in tetradecane viscosity for reference. At 20°C the sample shows a greater loss modulus than elastic modulus, indicating fluid-like behavior. When the temperature was heating up, a crossover between G' and G'' is observed at this frequency between 14 and 13°C. Note that both moduli increase rapidly over a fairly narrow range of frequencies and that the elasticity increases by nearly five orders of magnitude. The G' and G'' from the temperature sweep were represented as $\tan \delta$ to further assess the degree of solid-like behavior. We observed that at these lower temperatures, $\tan \delta$ is reasonably constant, and significantly less than 1, which is a typical characteristic of a gel [62, 63].

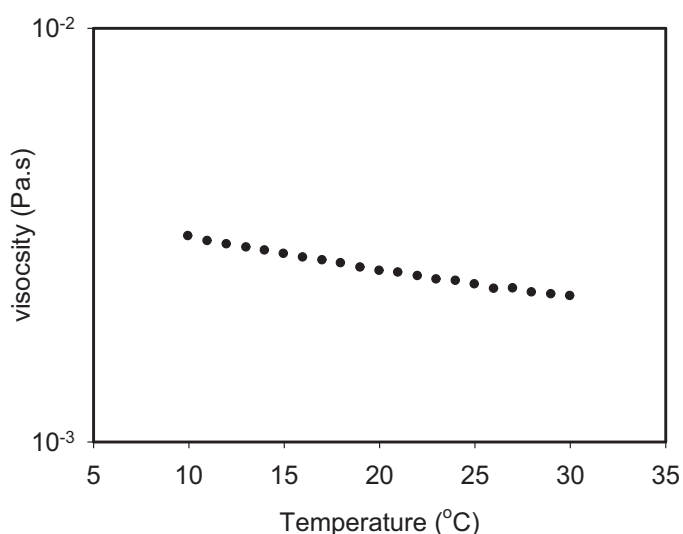


Figure 5.3 Temperature dependence of n-tetradecane

5.3 Frequency Sweep

The gel temperature determined from a temperature sweep measurement is dependent on the oscillatory frequency used, meaning such gel temperatures will change if

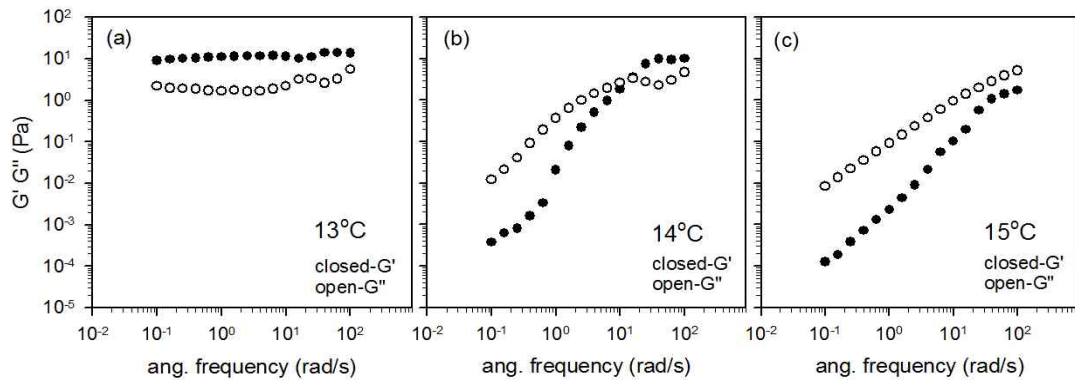


Figure 5.4 Frequency sweep measurements of 6 vol% AHE dispersion from 13°C to 15°C.

another frequency is used. So as a next step, we performed a frequency sweep to determine the temperature at which the system is solidlike across a sufficiently broad range of frequencies (i.e., for a sufficiently long window of time). Figure 5.4c shows that the sample exhibits liquid-like terminal behavior of a colloidal dispersion. Figure 5.4b shows that at 14°C, there is a crossover between G' and G'' at some frequency, indicating the system will flow at the time corresponding to the inverse of that frequency and for longer times, but is solid-like on shorter time scales. However, at 13°C, G' dominates over G'' at all frequencies, suggesting the system is solid-like for the time scales of interest, in this case, from 0.01s to 1s. At this temperature, G' and G'' are nearly parallel for the observed frequency range, which means that, according to the Winter and Chambon criteria [2], a gel-like structure has formed. The determination of the critical gel temperature requires further investigation by series of measurements with fine temperature tuning between 13°C to 14°C. For the purposes of this investigation, it is sufficient to note that gelation occurs at 6 vol% for AHE of aspect ratio 2.5 between 13 and 14 °C.

The behavior is qualitatively similar to that observed suspensions of spherical particles as reported by Kim et al. [15]. However, there is an important difference- Kim et al.

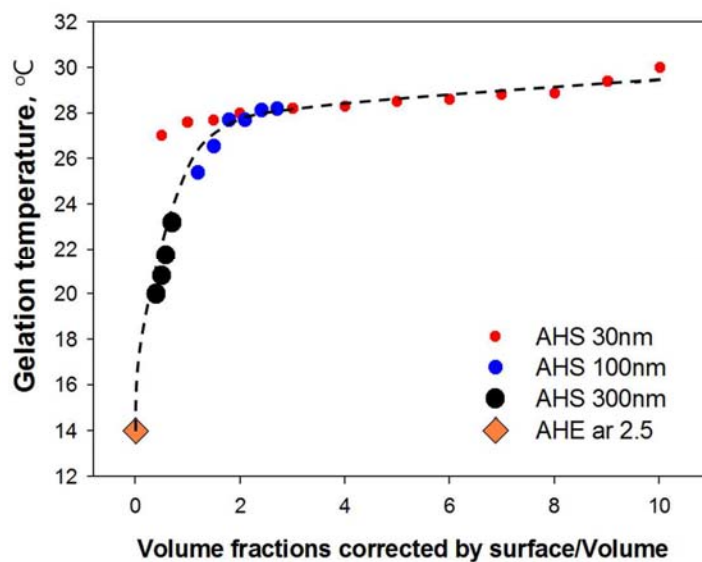
observed that corresponding attractive octadecyl-silica particles never formed a homogeneous gel 6 vol%, but rather, phase separated instead. They found that a stable gel forms at 14 vol%, which tells us that the phase behavior is strongly dependent on particle shape at a given particle volume fraction.

5.4 Comparison of the Gel Temperature with Spherical Systems

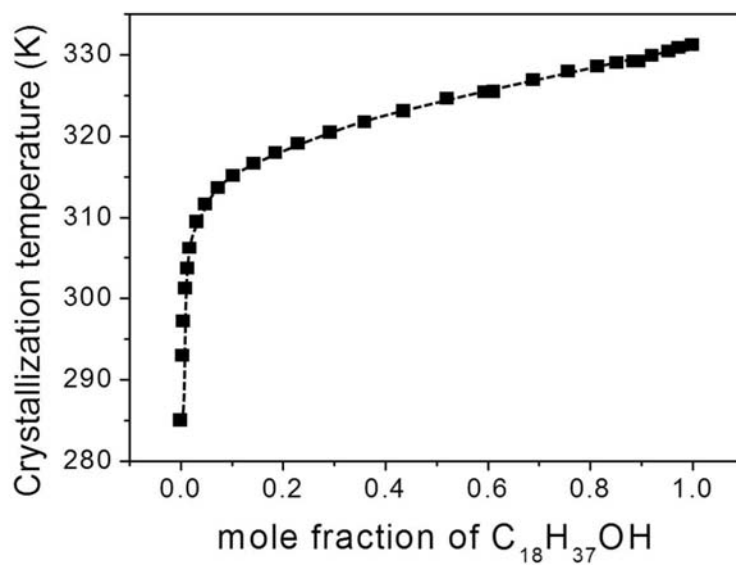
The gel temperature for this system is related to the crystallization of the brush layer because the particle attraction is induced by the molecular reconfiguration of the brush layer. Kim et al. observed some qualitative similarity between the gel temperatures of Adhesive Hard Spheres (with different particle sizes) and the crystallization temperatures of octadecanol in tetradecane [15]. In their analysis, they compared the gel temperature for different particle sizes and volume fractions in terms of the relative concentration of the brush molecules to the solvent. The gel temperature is found to be a universal curve when expressed in terms of the mole fraction of the brush layer relative to the solvent and brush layer in the system. They constructed a fitting function [64]:

$$T_{gel} = A\left(1 - \exp\left(-\frac{x}{x_0}\right)\right) + Bx \quad (5.1)$$

where x is the mole fraction of the octadecane chain layer in n -tetradecane, and A , x_0 , and B are fitting constants.



(a)



(b)

Figure 5.5 (a) Gel temperature comparison of three different particle sizes as a function of volume fraction. The data for spheres are adapted from [64]. (b) Crystallization temperature of a mixture of 1-octadecanol and n-tetradecane as a function of mole fraction of 1-octadecanol. The figure is reprinted from [64].

Figure 5.5 shows the rheologically determined gel temperature of the spherical systems of varying size and concentration and the AHE dispersion measured in this work as a function of mole fraction of the brush layer. The red, gold, and blue circles indicate the 30 nm, 100 nm, and 300 nm AHS particles and orange diamond indicates AHE particles, respectively. The trend line represented by the dashed line adequately describes the data as the orange diamond lies nicely onto the master curve within error estimates. The fit results in $A = 27.38 \pm 0.40$, $x_0 = 0.0042 \pm 0.0003$, and $B = 19.75 \pm 5.10$ with $R^2 = 0.920$ as reported in [64]. Kim et al. argued that the gel temperature is not only a function of volume fraction but also heavily affected by the available surface area in the unit volume. The fact that the gel temperature of ellipsoids follows the universal behavior of gelation of spherical particles supports a hypothesis that the gel transition depends on the available total surface area, or equivalently the mole fraction of the chain layer, and further, is independent of the particle shape. This surprising result is of great practical value as it shows that the gel temperature can be calculated from the correlation for both spheres and ellipsoidal particles for a given composition and surface to volume ratio.

Steady shear experiments on 6 vol% AHE suspensions were performed using a controlled stress rheometer (DHR, TA Instruments, Inc.) with a cone and plate geometry (40 mm cone diameter, 1 mm cone angle). Temperature during rheological measurement was maintained at 10 °C or 30 °C using peltier temperature control. The sample was pre-sheared for 1 minute at 500 s⁻¹ before measurements to eliminate any sampling history. Ascending and descending shear rate sweeps were performed on samples from 2 s⁻¹ to a maximum stress of 900 s⁻¹, collecting the viscosity values at each applied shear rate value. As shown in Figure 5.6, AHE suspension both 10 °C and 30 °C exhibit shear thinning behavior.

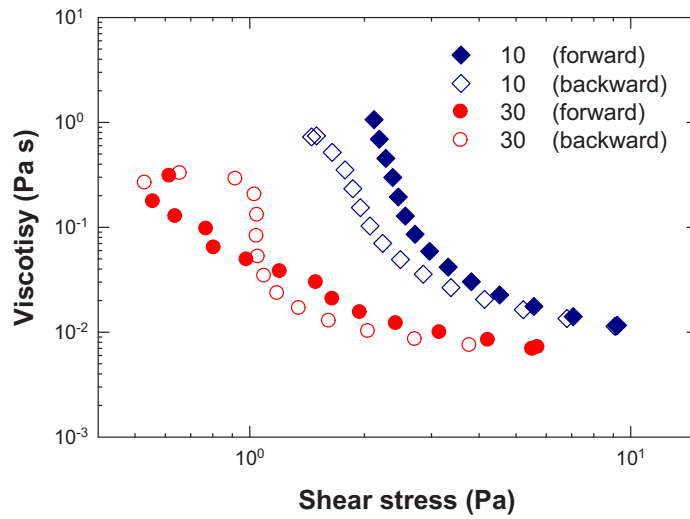


Figure 5.6 Ascending and descending shear stress sweeps performed for 6 vol% AHE suspension.

The fact that AHE suspension still exhibit shear thinning behavior at 10 °C is in contrast to observations for AHS particle suspensions [28]. The suspension shows a yield stress at 10 °C reflecting that it becomes a gel. At 30 °C, it does not show a yield stress implying that it is a suspension. At a high stress, shear thinning characteristics are shown for both temperatures. The shear thinning behavior may be caused by the alignment of particles in the flow direction due to particle-particle interaction under flow. We also note that there is some hysteresis in the forward and backward sweeps which is consistent with shear-induced changes in microstructure.

Chapter 6

SMALL-ANGLE NEUTRON SCATTERING RESULTS AND DISCUSSION

In this chapter, we will discuss small angle neutron scattering results of 6 vol% AHE suspension. SANS experiments were performed on the NG3 30m SANS instrument at NIST. For SANS measurements, the sample was loaded in a demountable titanium cell composed of a titanium frame holding quartz windows separated by a 1 mm path length. Measurements were made at detector distance configurations of 1 m, 4 m, and 13 m with lenses. The scattering time for each sample was 5 minutes, 10 minutes, and 15 minutes for 1 m, 4 m, and 13 m with lenses or 15 m, respectively. The transmission of each sample was measured at a fixed duration of 3 minutes per sample. Blocked beam and empty cell were also measured, which are needed to reduce the data to absolute scale. The reduction of the collected data was performed with the SANS Macros modules in Igor Pro [45].

Figure 6.1 show a distinct upturn in intensity at a low q suggesting that a three-dimensional percolated network structure spanning the whole sample volume is formed. The slope of the intensity at low q is approximately $-2.05 (\pm 0.03)$, which indicates that the observed system is a densely networked structure having the fractal dimension of 2.05. According to Kim et al, the fractal dimension obtained for spherical system is 1.7 for the 100 nm particle systems at 20 vol% [16]. Considering that corresponding sphere radius of AHE particle is 120 nm, this suggests that an anisotropic system forms a much denser microstructure compared to an isotropic system even at much lower volume fraction. Mohraz et al. [7] reported the similar aggregation behavior of rod type boehmite colloids and compared the results with a spherical particle suspension. They found that clusters composed of rods with aspect

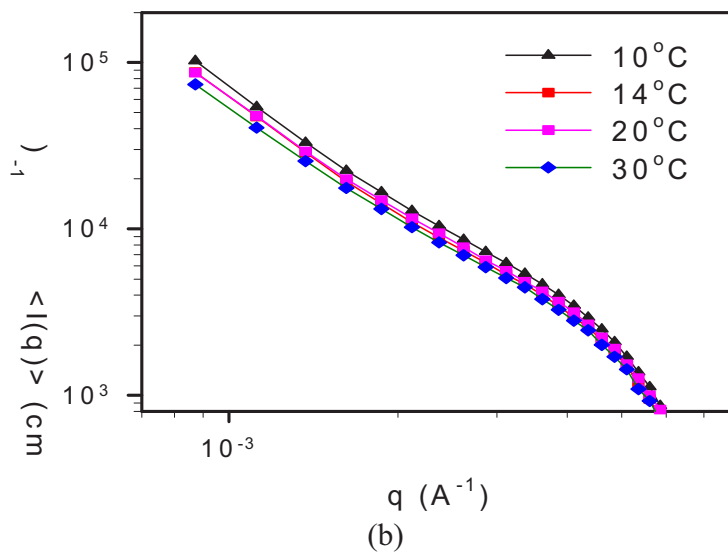
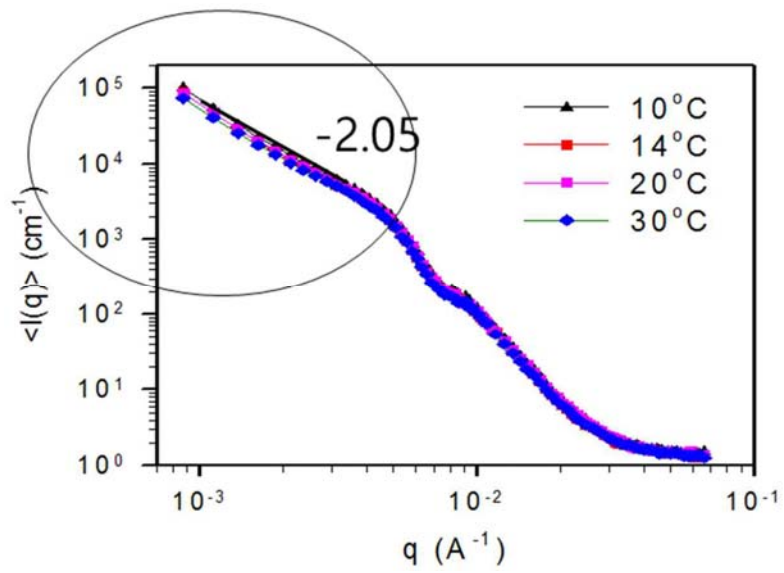


Figure 6.1 (a) 1-D SANS intensity curves of a dispersion of 6 vol% AHE particles in *n*-tetradecane from 10 °C to 30 °C. (b) Zoom-in of the low *q* region. Note: The data at 20 °C (purple points) are almost exactly overlapped on the data at 14 °C (Red points). Hence the data at 14 °C are not visible.

ratio 3.9 have a fractal dimension of $1.97 (\pm 0.05)$, which is similar to our observation. This network fractal dimension is affected by the shape of primary particles making up

the aggregates. As aspect ratio increases, a more branched and compact structure is formed in comparison with the structure of the aggregates formed by spherical particles.

The scattering intensity overlaps for the entire range of temperature meaning that the structure has no significant temperature dependence, which conflicts with the rheological data shown in chapter 3. When we see the zoom in intensities, however, there is a slight change at intensity that varies in a manner consistent with the rheological signature. A possible reason for this observation is that the van der Waals forces are already sufficient to induce a weak gel structure at high temperatures. Further cooling leads to a strengthening of the bonds between the ellipsoids without significant change in microstructure leading to an increase in the modulus. A similar effect was reported by Eberle et al. for the AHS system, where once the gel formed the structure did not change with further cooling despite large increases in the moduli [28,58]. Other plausible reasons could be that there are structural changes at longer length scales that are too large to detect with SANS. To test this further, USANS or SALS experiments are needed.

Chapter 7

CONCLUSION AND FUTURE DIRECTION

7.1. Conclusion

There are a lot of intriguing phenomena in suspensions of anisotropic as compared with isotropic particle suspensions. From this perspective, the present study focused on two primary objectives. The first objective was to synthesize and characterize a model system of chemically identical, anisotropic colloidal suspension having relatively mono-disperse ellipsoidal geometry in order to investigate the effects of particle anisotropy on dynamical arrest of adhesive hard particle system. The second objective was to explore the thermoreversible gelation in anisotropic particle suspensions via measuring the rheological response and directly probing the microstructure with small-angle neutron scattering (SANS).

The synthesis of well characterized, model anisotropic particle dispersions having uniform shape and low polydispersity is developed and demonstrated. Our model Adhesive Hard Ellipsoid particles consist of ellipsoidal titanium dioxide particles as the core coated with a silica shell and grafted with octadecyl brush. A coating of silica was added to achieve the same surface chemistry as the previous isotropic systems and to reduce the strength of the van der Waals attractions between the titanium oxide cores. The van der Waals energy between two core-shell ellipsoids in tetradecane was calculated and the based on orientation dependant van der Waals energy curve as a function of coating thickness, the optimum thickness was determined as 30nm for the model suspension. With this calculation as guidance, the methods given in the literature were modified to develop a successful synthesis of the model ellipsoid particles of aspect ratio of 2.5 and long axis of 210 nm. These particles were coated with octadecane and successfully dispersed in tetradecane.

The thermoreversible dynamic arrest of the AHE dispersions was examined by rheological characterization. The adhesive hard ellipsoid suspension formed a gel like structure upon cooling, as observed previously for the case of spherical particles. However, importantly the dispersions of AHE particles formed a gel at a lower volume fraction (6 vol%). When the gel temperatures for the AHS particles and AHE particle are plotted together as a function of the mole fraction of octadecyl brush to solvent, the gel temperature of ellipsoids follows the universal behavior of gelation of spherical particles. This universal behavior agrees with the hypothesis that the gel transition may be dependent on the available total surface area, or equivalently the mole fraction of the brush layer. Thus, gelation in these systems follows a master curve of the gel temperature as a function of the amount of brush molecules in the solvent. From this perspective, we conclude that particle shape does not affect the gel temperature for this system, but only the critical minimum gelation concentration depends on the particle aspect ratio. This makes sense if the strength of the adhesive interactions induced by brush crystallization acting between particles does not depend on the particle shape. However, the number of contacts acting between particles will depend on the particle shape such that suspensions of high aspect ratio particles will have more adhesive contacts than spherical particles for a given volume fraction, as long as the particles are randomly oriented and dispersed. Thus, the minimum volume fraction at which homogeneous gelation can occur should be dependent on the shape of the particles. This result is consistent with the theory of Kim et al. [16] where the critical gravitational Peclet number for gelation in spherical particles depends on the fractal dimension, such that a more open network with more contacts can form a gel at lower concentrations. Based on our findings, we can predict the absolute gel temperature from the gel geometric properties of adhesive hard particle system, but as of yet, cannot predict the minimum gel concentration. This study, however, cannot directly compare with AHS system due to the residual attractions evident even at higher temperatures from the van der Waals interactions between the dense titanium oxide cores.

7.2 Future Direction.

One goal of the research is to provide a universal state diagram for colloidal and molecular fluids with excluded volume and short range interactions, including the effect of particle shape. The adhesive hard ellipsoids studied in this thesis provided a good model system, but were shown to exhibit significant van der Waals attractions originating from TiO_2 particle core. Although a thermally reversible gel transition was demonstrated, because of this strong van der Waals force, AHE suspensions showed evidence of attractive forces between particles even at high temperatures (Figure A1). In Chapter 6, this van der Waals force acting between particles in suspension was shown to affect the suspension microstructure independent of the thermoreversible sol-gel transition. Therefore, it was not possible to determine the effective strength of interaction at the gel transition from the SANS data as no significant change in microstructure was evident over the length scales probed. Therefore, it is suggested that the development of silica ellipsoids without the core titanium oxide particle as a template could be a better route to study of the effect of particle anisotropy on gelation. Synthesis protocol of ellipsoids silica particles have been reported in the literature by Zhang et al. [65]. The development of model AHE particles based on ellipsoidal silica would provide a model system closer to the AHS system studied previously and allow for the quantitative study of the thermoreversible sol-gel transition in AHE suspensions.

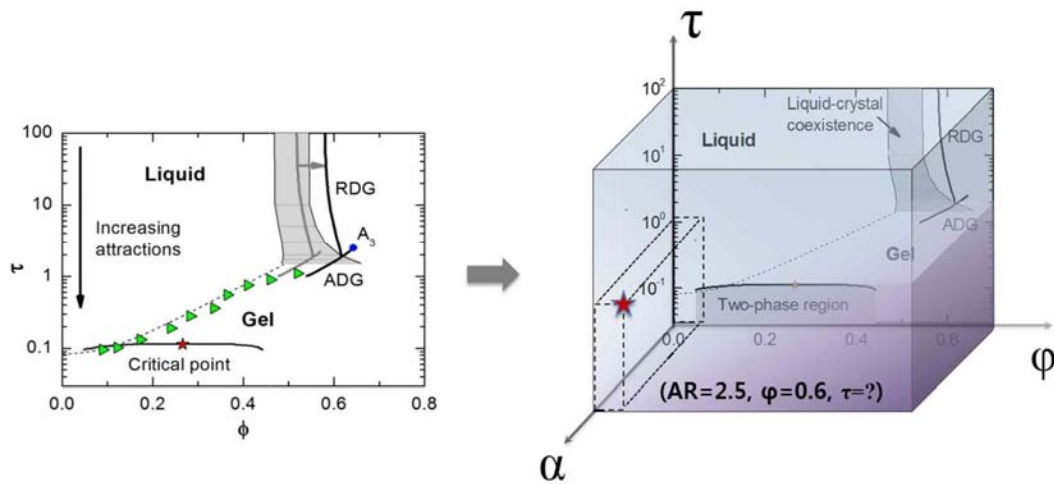


Figure 7.1 3D Proposed 3D state diagram for the adhesive hard ellipsoid model system (right) similar to that of isotropic system [6] (left) τ , ϕ , and α indicate Baxter parameter, volume fraction, and particle anisotropy, respectively.

This study will be continued to integrate the knowledge of static and dynamic behavior to formulate a theoretical and experimental 3-D phase diagram of the AHE at various aspect ratios, attractive forces, and ϕ regimes. The result will be compared with the spherical system. To explore the rheology and microstructural evolution under shear flows in anisotropic particle suspensions, combining rheology with small angle neutron scattering (flow-SANS) will enable quantifying the flow-induced alignment and other microstructural changes. The present study will be significant and fundamental importance to a broad range of investigators interested in soft matter, molecular thermodynamics, and rheology. Also, from an industrial perspective, they will directly benefit suspension formulation and manufacturing processes employing suspensions of anisotropic particle. This state diagram will then be used as a reference for studying dispersions of anisotropic particles.

REFERENCES

1. Eberle, A.P.R., N.J. Wagner, and R. Castaneda-Priego, *Dynamical Arrest Transition in Nanoparticle Dispersions with Short-Range Interactions*. Physical Review Letters. **106**(10): p. 105704.
2. Winter, H.H. and F. Chambon, *Analysis of linear viscoelasticity of a cross-linking polymer at the gel point*. Journal of Rheology, 1986. **30**(2): p. 367-382.
3. Mewis, J. and N.J. Wagner, *Colloidal suspension rheology*. 2012, New York: Cambridge University Press.
4. Egres, R.G. and N.J. Wagner, *The rheology and microstructure of acicular precipitated calcium carbonate colloidal suspensions through the shear thickening transition*. Journal of Rheology, 2005. **49**(3): p. 719-746.
5. Solomon, M.J. and P.T. Spicer, *Microstructural regimes of colloidal rod suspensions, gels, and glasses*. Soft Matter, 2010. **6**(7): p. 1391-1400.
6. Garboczi, E.J., et al., *Geometrical percolation-threshold of overlapping ellipsoids*. Physical Review E, 1995. **52**(1): p. 819-828.
7. Mohraz, A., et al., *Effect of monomer geometry on the fractal structure of colloidal rod aggregates*. Physical Review Letters, 2004. **92**(15).
8. Eberle, A.P.R., et al., *Dynamical Arrest, Percolation, Gelation, and Glass Formation in Model Nanoparticle Dispersions with Thermoreversible Adhesive Interactions*. Langmuir. **28**(3): p. 1866-1878.
9. Lu, P.J., et al., *Gelation of particles with short-range attraction*. Nature, 2008. **453**(7194): p. 499-504.
10. Solomon, M.J. and P. Varadan, *Dynamic structure of thermoreversible colloidal gels of adhesive spheres*. Physical Review E, 2001. **63**(5).
11. Trappe, V., et al., *Jamming phase diagram for attractive particles*. Nature,

2001. **411**(6839): p. 772-775.
12. Verduin, H. and J.K.G. Dhont, *Phase-diagram of a model adhesive hard-sphere dispersion*. Journal of Colloid and Interface Science, 1995. **172**(2): p. 425-437.
 13. Baxter, R.J., *Percus-Yevick equation for hard spheres with surface adhesion*. Journal of Chemical Physics, 1968. **49**(6): p. 2770-2774.
 14. Chiew, Y.C. and E.D. Glandt, *Percolation behavior of permeable and of adhesive spheres*. Journal of Physics A-Mathematical and General, 1983. **16**(11): p. 2599-2608.
 15. Kim, J.M., *Effect of the range of attraction on the rheology, microstructure, and thermodynamics of thermoreversible gels*. 2013, University of Delaware.
 16. Kim, J.M., et al., *Gel Transition in Adhesive Hard-Sphere Colloidal Dispersions: The Role of Gravitational Effects*. Physical Review Letters, 2013. **110**(20).
 17. Vavrin, R., et al., *Structure and phase diagram of an adhesive colloidal dispersion under high pressure: A small angle neutron scattering, diffusing wave spectroscopy, and light scattering study*. Journal of Chemical Physics, 2009. **130**(15): p. 154903.
 18. Sztucki, M., et al., *Kinetic arrest and glass-glass transition in short-ranged attractive colloids*. Physical Review E, 2006. **74**(5).
 19. Grant, M.C. and W.B. Russel, *Volume-fraction dependence of elastic-moduli and transition-temperatures for colloidal silica-gels*. Physical Review E, 1993. **47**(4): p. 2606-2614.
 20. Ramakrishnan, S. and C.F. Zukoski, *Microstructure and rheology of thermoreversible nanoparticle gels*. Langmuir, 2006. **22**(18): p. 7833-7842.
 21. Rueb, C.J. and C.F. Zukoski, *Rheology of suspensions of weakly attractive*

- particles: Approach to gelation*. Journal of Rheology, 1998. **42**(6): p. 1451-1476.
22. Eberle, A.P.R., et al., *Temperature-dependent nanostructure of an end-tethered octadecane brush in tetradecane and nanoparticle phase behavior*. Langmuir, 2010. **26**(5): p. 3003-3007.
 23. van Helden, A.K., J.W. Jansen, and A. Vrij, *Preparation and characterization of spherical monodisperse silica dispersions in non-aqueous solvents*. Journal of Colloid and Interface Science, 1981. **81**(2): p. 354-368.
 24. Roke, S., et al., *Surface molecular view of colloidal gelation*. Proceedings of the National Academy of Sciences of the United States of America, 2006. **103**(36): p. 13310-13314.
 25. Noro, M.G. and D. Frenkel, *Extended corresponding-states behavior for particles with variable range attractions*. Journal of Chemical Physics, 2000. **113**(8): p. 2941-2944.
 26. Bergenholtz, J. and M. Fuchs, *Nonergodicity transitions in colloidal suspensions with attractive interactions*. Physical Review E, 1999. **59**(5): p. 5706-5715.
 27. Valadez-Pérez, N.E., et al., *Dynamical arrest in adhesive hard-sphere dispersions driven by rigidity percolation*. Physical Review E. **88**(6): p. 060302.
 28. Eberle, A.P.R., et al., *Shear viscosity and structural scalings in model adhesive hard-sphere gels*. Physical Review E. **89**(5): p. 050302.
 29. Langmuir, I., *The Role of Attractive and Repulsive Forces in the Formation of Tactoids, Thixotropic Gels, Protein Crystals and Coacervates*. The Journal of Chemical Physics, 1938. **6**(12): p. 873-896.
 30. Lekkerkerker, H.N.W., et al., *Phase-Behavior of Colloid Plus Polymer*

- Mixtures*. Europhysics Letters, 1992. **20**(6): p. 559-564.
31. Bolhuis, P. and D. Frenkel, *Tracing the phase boundaries of hard spherocylinders*. The Journal of Chemical Physics, 1997. **106**(2): p. 666-687.
 32. Frenkel, D., *The hard ellipsoid-of-revolution fluid I. Monte Carlo simulations*. Molecular Physics, 1985. **55**(5): p. 1171-1192.
 33. Donev, A., *Unusually dense crystal packings of ellipsoids*. Physical Review Letters, 2004. **92**(25): p. 255506.
 34. Pfleiderer, P., *Simple monoclinic crystal phase in suspensions of hard ellipsoids*. Physical review. E, Statistical, nonlinear, and soft matter physics, 2007. **75**(2): p. 020402.
 35. Radu, M., P. Pfleiderer, and T. Schilling, *Solid-solid phase transition in hard ellipsoids*. The Journal of Chemical Physics, 2009. **131**(16): 020402.
 36. Mukhija, D. and M.J. Solomon, *Nematic order in suspensions of colloidal rods by application of a centrifugal field*. Soft Matter. **7**(2): p. 540-545.
 37. van der Kooij, F.M., K. Kassapidou, and H.N.W. Lekkerkerker, *Liquid crystal phase transitions in suspensions of polydisperse plate-like particles*. Nature, 2000. **406**(6798): p. 868-871.
 38. Dogic, Z., et al., *Isotropic-nematic phase transition in suspensions of filamentous virus and the neutral polymer Dextran*. Physical Review E, 2004. **69**(5): p. 051702.
 39. Solomon, M.J. and D.V. Boger, *The rheology of aqueous dispersions of spindle-type colloidal hematite rods*. Journal of Rheology (1978-present), 1998. **42**(4): p. 929-949.
 40. Egres, R.G., F. Nettesheim, and N.J. Wagner, *Rheo-SANS investigation of acicular-precipitated calcium carbonate colloidal suspensions through the shear thickening transition*. Journal of Rheology, 2006. **50**(5): p. 685-709.

41. Berne, B.J.P., R., *Dynamic Light Scattering*. 2000: Courier Dover Publications.
42. Rasband, W.S., *ImageJ* 2009, National Institute of Health. p. <http://rsb.info.nih.gov/ij/>.
43. Hammouda, B., *Probing nanoscale structures – the SANS toolbox*. 2012, National Institute of Standards and Technology: Pre-print.
44. *SasView*. [cited; Available from: <http://www.sasview.org/>].
45. Kline, S.R., *Reduction and analysis of SANS and USANS data using IGOR Pro*. *Journal of Applied Crystallography*, 2006. **39**: p. 895-900.
46. Eberle, A.P.R. and L. Porcar, *Flow-SANS and Rheo-SANS applied to soft matter*. *Current Opinion in Colloid & Interface Science*, 2012. **17**(1): p. 33-43.
47. Porcar, L., et al., *Rheo-small-angle neutron scattering at the National Institute of Standards and Technology Center for Neutron Research*. *Review of Scientific Instruments*, 2011. **82**(8).
48. Russel, W.B., Saville, D.A. and Schowalter, W.R., *Colloidal Dispersions*. 1989: Cambridge University Press.
49. Viravathana, P. and D.W.M. Marr, *Optical trapping of titania/silica core-shell colloidal particles*. *Journal of Colloid and Interface Science*, 2000. **221**(2): p. 301-307.
50. Moon, P.H. and D.E. Spencer, *Field theory handbook; including coordinate systems, differential equations, and their solutions*. 1961, Berlin: Springer-Verlag.
51. Sugimoto, T., X.P. Zhou, and A. Muramatsu, *Synthesis of uniform anatase TiO₂ nanoparticles by gel-sol method 4. Shape control*. *Journal of Colloid and Interface Science*, 2003. **259**(1): p. 53-61.
52. Sacanna, S., et al., *Fluorescent monodisperse silica ellipsoids for optical*

- rotational diffusion studies*. Langmuir, 2006. **22**(4): p. 1822-1827.
53. Rueb, C.J. and C.F. Zukoski, *Viscoelastic properties of colloidal gels*. Journal of Rheology, 1997. **41**(2): p. 197-218.
 54. Rahtu, A. and M. Ritala, *Reaction Mechanism Studies on Titanium Isopropoxide/Water Atomic Layer Deposition Process*. Chem. Vap. Deposition Chemical Vapor Deposition, 2002. **8**(1).
 55. *CRC Handbook of Chemistry and Physics*. 2011-2012, Taylor and Francis Group, LLC.
 56. van Bruggen, M.P.B., *Preparation and Properties of Colloidal Core-shell Rods with Adjustable Aspect Ratios*. Langmuir, 1998. **14**(9): p. 2245-2255.
 57. Graf, C., et al., *A General Method To Coat Colloidal Particles with Silica*. Langmuir, 2003. **19**(17): p. 6693-6700.
 58. Eberle, A.P.R., et al., *Dynamical Arrest, Percolation, Gelation, and Glass Formation in Model Nanoparticle Dispersions with Thermoreversible Adhesive Interactions*. Langmuir, 2012. **28**(3): p. 1866-1878.
 59. Eberle, A.P.R., N.J. Wagner, and R. Castaneda-Priego, *Dynamical arrest transition in nanoparticle dispersions with short-range interactions*. Physical Review Letters, 2011. **106**(10): p. 105704.
 60. de Miguel, E., et al., *Effect of the attractive interactions on the phase behavior of the Gay-Berne liquid crystal model*. The Journal of Chemical Physics, 1996. **105**(10): p. 4234-4249.
 61. Winter, H.H., et al., *An empirical constitutive law for concentrated colloidal suspensions in the approach of the glass transition*. Rheologica Acta, 2009. **48**(7): p. 747-753.
 62. Horst, R.H. and H.H. Winter, *Stable critical gels of a crystallizing copolymer*

- of ethene and 1-butene*. *Macromolecules*, 2000. **33**(1): p. 130-136.
63. Soenen, H., et al., *Ordering and structure formation in triblock copolymer solutions .1. Rheological observations*. *Polymer*, 1997. **38**(22): p. 5653-5660.
64. Kim, J.M., *Effet of the range of attraction on the rheology, microstructure, and thermodynamics of thermoreversible gels with adhesive hard-sphere interactions* in *Department of Chemical Engineering*. 2013, the University of Delaware: Newark.
65. Zhang, H., T.J. Bandosz, and D.L. Akins, *Template-free synthesis of silica ellipsoids*. *Chemical Communications*. **47**(27): p. 7791-7793.

Appendix

NOMENCLATURE AND ACRONYMS

| Symbol | SI units | definition |
|--------------|---|--|
| a | [m] | Particle radius |
| A | [kgm ⁻² s ⁻²] | Hamaker constant |
| B_2 | [m ³] | Second virial coefficient |
| d | [m] | Surface-to-surface distance |
| df | | Mass-fractal dimension |
| D_h | [m] | Effective hydrodynamic particle diameter |
| g | [ms ⁻²] | Gravitational acceleration |
| G' | [kgms ⁻²] | Storage modulus |
| G'' | [kgms ⁻²] | Loss modulus |
| $I(q)$ | [m ⁻¹] | Scattering intensity |
| k_B | [kgm ² s ⁻² K ⁻¹] | Boltzman constant |
| m | [kg] | Mass |
| n | | Refractive index |
| $P(q)$ | | Static form factor |
| q | [m ⁻¹] | Scattering vector |
| r | [m] | Center-to-center interparticle distance |
| R_g | [m] | Radius of gyration |
| $S(q)$ | | Static structure factor |
| t | [s] | time |
| T | [K] | Temperature |
| γ | | strain |
| δ | | Phase angle |
| η | [kgs ⁻¹ m ⁻¹] | viscosity |
| v | [ms ⁻¹] | Sedimentation velocity |
| ρ | [kgm ³] | density |
| ρ_{SLD} | [m ⁻²] | Scattering length density |
| τ | [kgm ² s ⁻²] | Torque |
| ϕ | | Volume fraction |
| ω | [s ⁻¹] | Oscillatory frequency |